Energy 336 (2025) 138380

Contents lists available at ScienceDirect

Energy

journal homepage: www.elsevier.com/locate/energy

Techno-economic optimization of an integrated ammonia–methane synthesis system powered by LNG-assisted biogas oxy-fuel cycle and vanadium chloride hydrogen production

Shayan Sharafi Laleh [a], Shayan Rabet [a], Haniyeh Sadat Rezaei Mousavi [a], Mortaza Yari [a,*], Saeed Soltani [b], Ali Saberi Mehr [c,**]

[a] Faculty of Mechanical Engineering, University of Tabriz, 16471, Tabriz, Iran
[b] Faculty of Engineering and Natural Sciences, Antalya Bilim University, 07190, Antalya, Turkey
[c] School of Mechanical & Materials Engineering, University College Dublin, Dublin, Ireland

ARTICLE INFO

Handling Editor: Ruzhu Wang

Keywords:
Cryogenic air separation
Oxy-fuel combustion
Vanadium chloride
Ammonia synthesis
Methane production

ABSTRACT

This study presents a novel multi-generation biogas-fueled power system integrating oxy-fuel combustion and thermochemical hydrogen production for simultaneous power generation, synthetic fuel production, and carbon management. The system combusts biogas with pure oxygen, produced via cryogenic air separation using LNG cold energy, in three sequential combustion chambers and turbines. High-temperature exhaust gases are directed to a vanadium chloride (VCl) thermochemical cycle for hydrogen production and an Organic Rankine Cycle (ORC) for additional power recovery. At the same time, radiative heat from the combustion chambers is converted to electricity through thermophotovoltaic (TPV) units. Separated hydrogen is divided between methanation and ammonia synthesis units, using CO_2 from the final exhaust and nitrogen from air separation. Thermodynamic, techno-economic, and environmental analyses were conducted, followed by a multi-objective optimization using the Gray Wolf Optimizer. One scenario targeted maximum net power and exergetic efficiency with minimized product cost, another emphasized environmental impact reduction, and the third balanced subsystem exergetic efficiency with product cost. In the first case, the system achieved a net power output of 12,023.05 kW, an exergetic efficiency of 47.60 %, and a product cost of 19.21 $/GJ. The environmental-focused case reduced the environmental index to 0.4063 $/kWh with a product cost of 19.50 $/GJ, while the balanced case reached an exergetic efficiency of 45.23 %, a product cost of 19.12 $/GJ, and an environmental index of 0.4030 $/kWh. Increasing ammonia and methane prices to 1.6 $/kg and 0.6 $/kg shortened the payback period from 5.71 to 4.5 years. These results demonstrate the system's high efficiency, economic resilience, and renewable energy potential.

Nomenclature

Symbols and abbreviations		Greek symbols	
A	Area [m^2]	ρ	Electrical resistivity [Ω. m]
AI	Annual Income [$]	η_{exergy}	Efficiency of exergy [%]
bl	Plant lifetime [years]	η_c	Electrical conversion efficiency[%]
CC	Combustion Chamber	ε	Effectiveness factor [%]
CETD	Cold end temperature difference [K]	ϕ_r	Maintenance factor
CEPCI	Cost index	λ	Wavelength [μm]
CRF	Capital recovery factor	μ	Molar amounts of products
Comp	Compressor	**Subscripts**	
CV	Control volume	0	Reference condition
D	Diameter [m]	ch	Chemical
EES	Engineering equation solver	el	electrical
$\dot{E}x$	Exergy rate [kW]	em	emitter
$\dot{E}x_D$	Exergy destruction rate [kW]	en	Energy
FF	Fill factor	ex	Exergy

(continued on next column)

(continued)

(continued on next page)

* Corresponding author.
** Corresponding author.
E-mail addresses: myari@tabrizu.ac.ir (M. Yari), ali.saberimehr@ucd.ie (A. Saberi Mehr).

https://doi.org/10.1016/j.energy.2025.138380
Received 19 July 2025; Received in revised form 20 August 2025; Accepted 5 September 2025
Available online 8 September 2025

(*continued*)

GT	Gas Turbine	flt	filter
HEX	Heat Exchanger	in	Inlet
I_b	Blackbody radiative intensity [W/m^2]	imp	Impurities
IF	Inflation rate [%]	is	Isentropic
h	Specific enthalpy [kJ/kg]	net	Net
i_r	Interest rate [%]	ohm	Ohmic
K	Equilibrium constant	OM	Operate and maintain
LHV	Lower heating value [MJ/kg]	out	Outlet
LNG	Liquid Natural Gas	ph	Physical
$\dot{m}$	Mass flow rate [kg/s]	Pump	Pump
Mix	Mixer	q	Heat transfer rate
MSW	Municipal Solid Waste	rad	radiation
MOGWO	Multi-Objective Gray Wolf Optimization	ref	reflect
N	Yearly operational duration [hours]	th	Thermal
NPV	Net Present Value [M$]	tot	total
P	Pressure [kPa]	w	wall
PBP	Payback Period [year]		
PEC	Purchase Equipment Cost [$]		
$\dot{Q}$	Heat transfer rate [kW]		
Ri	Real Interest rate [%]		
s	Specific entropy [kJ/kg, K]		
Sep	Separator		
T	Temperature [K]		
TPV	Thermophotovoltaic		
Turb	Turbine		
VCl	Vanadium Chloride		
V_{oc}	Open-circuit voltage [V]		
$\dot{W}$	Power [kW]		
$\dot{Z}$	Investment cost rate [$/year]		

1. Introduction

1.1. Preface

The worldwide sector of energy sector is experiencing a shift due to boosting consumption from growth in populations, a prosperous economy, and urbanization, underscoring the necessity of ecologically sound, viable alternatives to energy [1]. In light of the global warming issue and the energy disasters, creative technological avenues are essential to mitigate carbon footprints and guarantee sustainability over the long run [2]. Sustainable sources of energy are rapidly becoming essential for promoting energy effectiveness, alleviating adverse environmental effects, and adhering to the world's sustainability desires [3]. Meanwhile, the combination of renewable energy sources with the fabrication of hydrogen, ammonia, and methane can augment their functionality, guaranteeing productivity and ecological sustainability [3].

1.2. Previous works

As noted by Shan et al. [4], these modelled a TPV–Brayton–Rankine cycle with different O_2 levels, fuels, and fluids. They uncovered n-pentane hit 30–32 % efficacy, fuel oil was 1–2 % more efficient than CH4, and oxy-fuel integration higher effectiveness by 2–3 %.

In order to achieve a zero CO_2 footprint, Cao et al. [5] constructed a CCHP plant that used methanation, cryogenic CO_2 recovery, and geothermal energy. In comparison with legacy generation, the levelized power price was 16.65 $/MWh, an drop of 87.6 %. The energy and exergy efficiencies were 30.87 % and 48.61 %, resp.

The positive aspects of staged TPV and chute energy utilization are highlighted by Shan et al. [6], who disclose that photo-thermal descend converter with oxy-fuel combustion may boost efficiency by 20 points for ultra-supercritical, 15 for combined cycle, and 30 for small organic Rankine cycles.

Using CO_2 hydrogenation and biomass, Eisavi et al. [7] evolved a comprehensive low-carbon method for the generation of electricity, CH_4, and methanol. ORC, PEM, a molten carbonate fuel cell, and synthesis units were all part of the structure. Regarding the levelized expense of 37.6 $/MW.hr for power, 92.8 $/MW.hr for methanol, and 79.4 $/MW.hr for CH_4, the energy efficiency was 36.8 %. Optimization increased energy efficiency to 34.8 % and down the CH_4 fee to 77.3 $/MW.hr.

Ghiasirad et al. [8] evaluated a biogas-to-fuels system combining anaerobic digestion, high-temperature electrolysis, biogas upgrading, LNG cold energy recovery, oxy-fuel gas turbine, and exhaust gas recycling to produce biomethane and biomethanol. Using Aspen Plus, Engineering Equation Solver, and SimaPro, they assessed energy, exergy, economic, and environmental performance, finding that LNG and gas turbine integration raised exergy efficiency from 85.07 % to 94.4 %, cut CO_2 emissions by 53 %, reduced resource use by 70 %, and shortened payback from 10 to 3 years. Gholizadeh et al. [9] analyzed a biofuel production system integrating anaerobic digestion of biomass with amine scrubbing CO_2 capture for biomethane and biomethanol synthesis. The process was simulated in Aspen Plus, with performance assessed through energy and exergy analyses, techno-economic evaluation, and life cycle assessment (LCA) using the Impact 2002+ method. The study compared systems with and without CO_2 capture, showing that the capture-integrated configuration achieved higher overall exergy efficiency (up to 80 %), significantly reduced greenhouse gas emissions (by over 70 %), and improved economic feasibility by lowering the levelized cost of biomethanol production. A wind-solar-biomass system for supplying NH_3, electricity was pitched by Khoshgoftar Manesh et al. [10], who obtained energy and exergy efficiencies of 31.33 % and 38.53 %, respectively. Optimized savings by 15.86 % and surged energy efficiency by 1.72 %. With a period of payoff of 3.29 years, the system delivered 275.44 tons of NH_3 and 18.51 MW. Pirmohamadi et al. [11] outlined a Brayton-based multigeneration unit inspired by NH_3-CH_4, achieving a thermal effectiveness of 56.5 % and an electric output of 17 MW. The setup produces 0.058 kg of CO_2 per kWh, with internal NH_3 and CH_4 generation accounting for 0.37 % and 9 % of the fuel, underscoring its ecological impact and energy conservation efforts. A green energy concept that integrates H_2 and NH_3 storage emerged by Chen et al. [12] after contrasting the plasma NH_3 synthesis and Haber-Bosch processes. When compared with the plasma technique to Haber-Bosch, the former produced a 19.8 % payback and a levelled cost of 0.062 $/kW.hr. Based on a sensitivity analysis, it might cost less than Haber-Bosch. Onwuemezie et al. [13] proposed a sustainable steel manufacturing method utilizing H_2, leading to a drop of CO_2 by 1111.4 kg every 626 kg of steel. The process boosts energy efficiency by more than 10 %, yields 61.1 kW from wasted heat, and saves 1290.4 kg/h of H_2, facilitating zero-emissions steel extraction. To be able to make electricity, H_2, NH_3, heating, cooling, drying, and hot water, Tukenmez et al. [14] constructed a multigeneration framework to include Rankine, ORC, and NH_3 and H_2 production subsystems. High reliability of the system was confirmed by energy and exergy efficiencies of 62.18 % and 58.37 %, as well. Eisavi et al. [15] set up a low-carbon multigeneration procedure taking advantage of municipal solid waste, attaining energy and exergy efficiencies of 41 % and 36 %, respectively. It delivers 179 tons of CH_4 and 393 tons of methanol per year, though implementing 1012 tons of CO_2, resulting in an environmental durability rating of 1.57.

Despite significant advances in multigeneration systems, existing studies have generally focused on limited subsystem combinations such as ORC–LNG–PEM integration, geothermal–cryogenic CO_2 recovery, or biomass-based carbon capture and fuel synthesis. While these configurations have improved thermodynamic or economic performance, none have achieved full integration of staged oxy-fuel combustion with LNG-driven cryogenic air separation, vanadium chloride thermochemical hydrogen production, thermophotovoltaic (TPV) units, and a closed-loop carbon utilization process within a single biogas-fueled platform. Furthermore, most prior works have optimized only one or two performance aspects—typically energy efficiency or cost—without

simultaneously considering environmental metrics in a multi-objective framework. This gap limits the ability to fully exploit synergies between advanced combustion control, cryogenic integration, multi-path heat recovery, and renewable fuel synthesis. The present study addresses this shortcoming by introducing and optimizing a unified architecture that maximizes product diversity and system performance while minimizing environmental impact.

Table 1 breaks down the most comparable subsystem combinations to the current study and contrasts their analytical approaches and findings with the findings from our investigation.

1.3. Merits of the study

This study introduces a pioneering biogas-fueled multi-generation system that unites advanced combustion, heat recovery, and renewable fuel synthesis within a single, tightly integrated architecture. The design is centered on sequential staged oxy-fuel combustion with controlled water injection, enabling precise flame temperature management and exhaust tailoring for downstream processes. It uniquely incorporates liquefied natural gas (LNG) cold energy to drive cryogenic air separation, producing oxygen for combustion and nitrogen for ammonia synthesis while significantly reducing parasitic energy loads. High-temperature exhaust streams are strategically distributed to multiple energy recovery paths, including expansion in gas turbines, thermochemical hydrogen production via the vanadium chloride (VCl) cycle, Organic Rankine Cycles (ORCs) for supplementary power, and thermophotovoltaic (TPV) units for direct radiative-to-electric conversion. Carbon dioxide from oxy-combustion is captured and combined with renewable hydrogen in a closed-loop methanation process, while hydrogen is also allocated for ammonia synthesis, maximizing product diversity. The system is comprehensively evaluated through thermodynamic, techno-economic, and environmental analyses, and is further refined through multi-objective optimization using the Gray Wolf Optimizer (GWO), ensuring an optimal balance of efficiency, cost, and environmental performance.

1.3.1. Key novel aspects

- **Sequential staged oxy-combustion with water injection** – Enables precise temperature control, staged energy recovery, and tailored exhaust for integration with multiple downstream processes.
- **Integration of LNG cold energy** – Powers cryogenic air separation, delivering oxygen for combustion and nitrogen for ammonia synthesis while boosting overall energy efficiency.
- **Multi-path energy recovery** – Exhaust heat simultaneously utilized in gas turbines, VCl hydrogen production, ORCs, and TPV units, minimizing exergy destruction.
- **Closed-loop carbon utilization** – Captured CO_2 is fully recycled via methanation with renewable hydrogen, approaching near-zero direct emissions.
- **Dual hydrogen pathways** – Hydrogen from the VCl cycle is split between methane and ammonia production, increasing the versatility and value of system outputs.
- **Comprehensive multi-objective optimization** – GWO used to maximize efficiency, minimize product cost, and optimize fuel/chemical production alongside environmental indicators.
- **First-of-its-kind integration** – Combines VCl thermochemical hydrogen production with staged oxy-fuel combustion and TPV-based radiative recovery in a biogas-powered platform for the first time.

1.3.2. Research objectives

This study aims to (i) demonstrate the feasibility of integrating staged oxy-fuel combustion, LNG-driven cryogenic air separation, and VCl thermochemical hydrogen production in a unified biogas-powered platform, (ii) evaluate its thermodynamic, economic, and

Table 1
Analysis strategies, achievements, and relevant subsystem schemes are compared to the present research.

No.	Subsystems	Outputs	Analytical Techniques	Ref.
1	Ammonia synthesis – Methanation – Vanadium Chloride cycle – ORC – oxyfuel combustion – Brayton cycle – LNG cryogenic air separation – TPV - Digestion	CH_4, NH_3, Heating, liquefied CO_2, N_2, Power, LNG	Energy, Exergy, Techno-economic, Economic, Environmental, Parametric study, Optimization (GWO)	This work
2	gas-cooled reactor - vanadium chloride cycle - biomass	hydrogen - power	energy - exergy – parametric study - sensitivity analysis	[16]
3	biomass gasifier - vanadium chloride cycle	hydrogen - power - CO_2 reduction	energy - exergy - environmental - optimization using deep learning	[17]
4	TPV - oxy-fuel combustion - Brayton cycle - Rankine cycle	power - heat recovery	thermodynamic analysis - parametric study	[18]
5	vanadium-chlorine cycle - Brayton cycle - biomass gasification	hydrogen - power - CO_2 reduction	energy - exergy - exergoeconomic - exergoenvironmental - multi-objective optimization evolutionary algorithm in MATLAB - parametric study	[19]
6	ammonia synthesis - ORC - waste heat recovery	ammonia - power	energy - exergy - economic - multi-scenario comparison - working fluid optimization with genetic algorithm	[20]
7	digestion – biogas – water-gas shift reaction – cryogenic air separation – ammonia synthesis	ammonia – hydrogen – methane	energy – exergy – sensitivity analysis	[21]
8	biomass gasification — electrolysis – methanation – LNG synthesis	Substitute Natural Gas – renewable liquefied natural gas (Green LNG) – hydrogen	techno-economic	[22]
9	biogas separation unit – LNG – ammonia Rankine cycle – desalination unit – Kalina cycle – SOEC – biomethane combined cycle – methanol synthesis unit	power – cooling – heating – fresh water – liquid CO_2 – biomethane – methanol	energy - exergy – economic – environmental analysis	[23]
10	Biomass – TPV	power – heating	energy – exergy – thermo-physical – parametric study	[24]
11	biogas - cryogenic separation – Kalina cycle – ORC – multi-effect desalination (MED) – LNG regasification	power – heating – fresh water – liquid CO_2 – biomethane	energy – exergy – environmental– economic	[25]

(continued on next page)

Table 1 (*continued*)

No.	Subsystems	Outputs	Analytical Techniques	Ref.
12	biomass gasification – hydrogen production – ammonia synthesis – Allam cycle (CO_2 capture) - oxy-combustion unit	power – ammonia – CO_2 captured	energy – exergy –comparative study	[26]

environmental performance under various operating scenarios, and (iii) identify optimal design and operating parameters through multi-objective optimization, targeting high efficiency, low environmental impact, and strong economic viability.

2. System description

As shown in Fig. 1, an integrated power generation and fuel synthesis system based on biogas combustion is proposed and evaluated. Biogas is produced via anaerobic digestion and subsequently compressed through a three-stage compression system to reach the required pressures for sequential combustion processes. Simultaneously, ambient air undergoes three-stage compression and is directed to a cryogenic separation unit, where oxygen is separated from nitrogen using the cold energy of liquefied natural gas (LNG). The separated oxygen is then preheated and utilized in an oxy-fuel combustion configuration.

The system comprises three sequential combustion chambers. In each chamber, biogas and oxygen are combusted in a controlled oxy-fuel environment, with flame temperatures regulated at approximately 1800 K through direct water injection. To prevent complete combustion in the first two stages and maintain sufficient oxygen for subsequent chambers, excess oxygen is retained in the exhaust gases. Each combustion

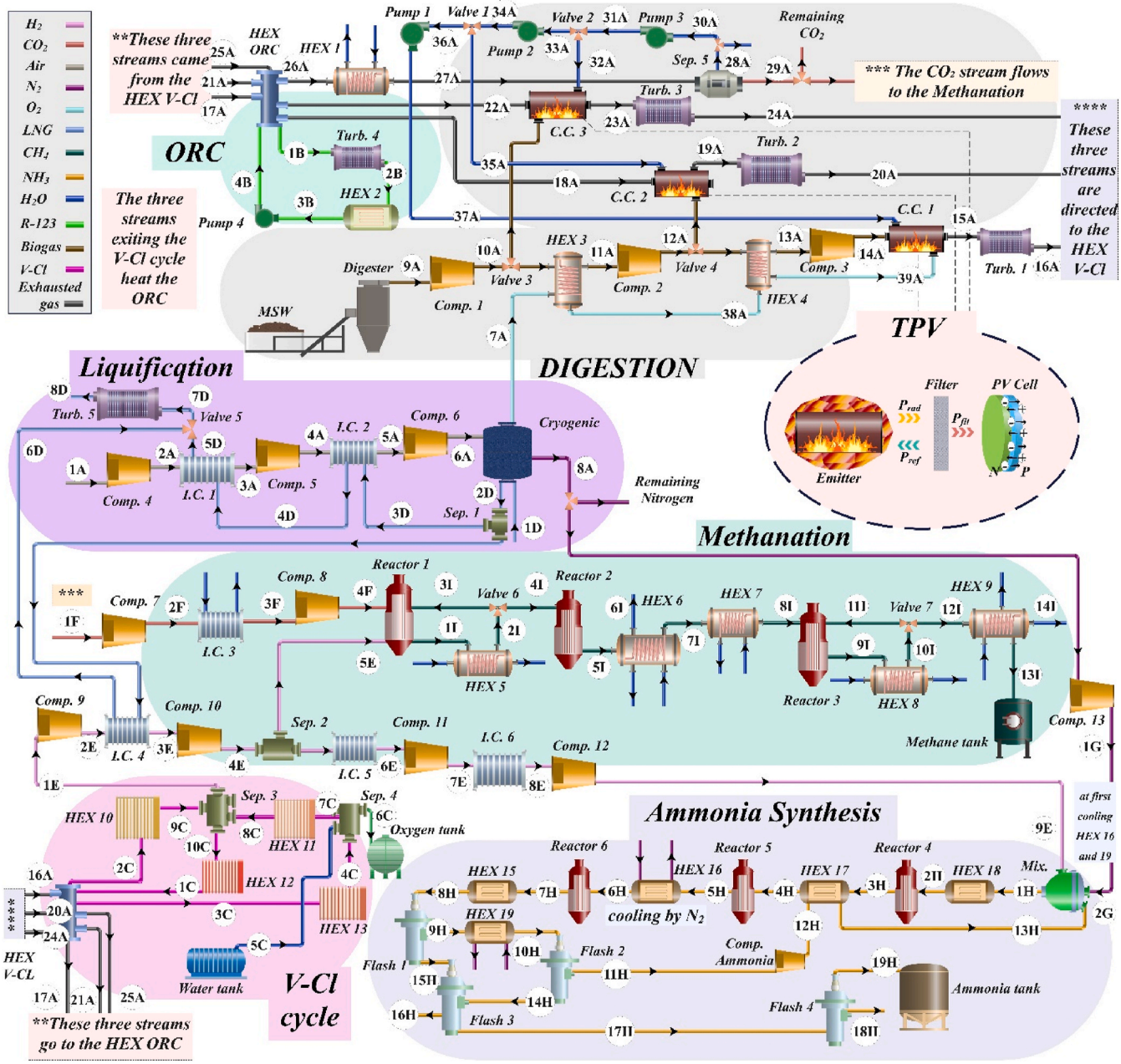

Fig. 1. The system configuration.

chamber is assumed to experience radiative heat losses equivalent to 5 % of the lower heating value (LHV) of the biogas. These radiative losses are partially recovered via thermophotovoltaic (TPV) units, which convert radiative heat into electrical power.

The high-temperature exhaust gas from each combustion chamber expands through a dedicated gas turbine, generating mechanical power. Post-expansion, the exhaust gas is employed to provide thermal energy to a vanadium chloride (VCl) thermochemical cycle for hydrogen production. The remaining heat is subsequently recovered in an organic Rankine cycle (ORC) for additional power generation before the exhaust stream is routed to the next combustion chamber.

In the third and final combustion chamber, the remaining oxygen is fully consumed with additional biogas, and the resulting exhaust gas, devoid of nitrogen due to the oxy-fuel configuration, undergoes final heat recovery through a gas turbine, VCl cycle, and ORC. The cooled final exhaust stream, containing primarily CO_2 and H_2O, is processed to separate water and capture CO_2.

The water separated from the final exhaust is recycled and injected into each combustion chamber to regulate flame temperatures. The captured CO_2 is directed to a methanation unit, where it reacts with a portion of the hydrogen produced by the VCl cycle to synthesize methane. The nitrogen separated from air during cryogenic separation is compressed and preheated, then combined with another portion of the produced hydrogen in an ammonia synthesis unit to generate ammonia.

3. System modeling

In this research, the proposed configuration was simulated through the Engineering Equation Solver (EES) platform to carry out detailed analyses of energy and exergy performance, alongside evaluations of economic feasibility and environmental impact. Subsequently, a multi-objective optimization process was implemented in MATLAB utilizing the Gray Wolf Optimization (GWO) algorithm, aimed at exploring the balance between conflicting goals. The fundamental thermodynamic modeling assumptions are outlined in Table 2, while further assumptions integrated into the simulation framework are as follows.

- The system operates under steady-state conditions [27].
- Kinetic and potential energy effects are neglected [27].
- The main thermal exchange within the vanadium chloride cycle takes place in Separator 1 during the initial step, whereas the heat transfer occurring in the following separators and associated heat exchangers is relatively less significant [28].

Table 2 presents the critical input data and thermophysical characteristics utilized in simulating and modeling the proposed hybrid configuration, encompassing parameters such as operating pressures and temperatures, component compositions, and efficiency metrics for major system elements.

3.1. Thermodynamic analysis

Table 3 provides a detailed summary of the fundamental equations governing energy and exergy balances, as well as mass flow allocation within the proposed system. It details the input and output flows for each subsystem, ensuring strict adherence to the conservation laws of mass, energy, and exergy across the entire configuration [41,42].

3.2. Digestion units

The digestion process was carried out using a thermophilic anaerobic reactor maintained at a constant temperature of 328.15 K. To maintain stable microbial performance, temperature fluctuations are typically considered negligible. The biogas generation analysis focuses exclusively on the volatile (ash-free) portion of Municipal Solid Waste (MSW), following the methodology proposed by Zhang et al. [29]. The formula used to represent biomass decomposition is provided below [43]:

$$C_nH_aO_b + wH_2O \rightarrow n_1CO_2 + n_2CH_4 \quad (1)$$

According to this study, approximately 95 % of the biomass is composed of volatile matter, of which around 70 % is biologically degradable and can be transformed into biogas through anaerobic microbial processes. The remaining fraction exits the digester as liquid

Table 2
Input parameters and thermodynamic properties used in the modeling.

Parameter	Value	Unit	Reference
Reference pressure, P_0	101.3	*kPa*	[8]
Reference temperature, T_0	25	$^\circ C$	[8]
Digestion unit			
Pressure ratio of compressors, PR_{comp}	16	–	[29]
Pressure ratio of pumps, PR_{pump}	16	–	[29]
Isentropic efficiency of turbines, $\eta_{is,Tur}$	89	%	[30]
Isentropic efficiency of compressors, $\eta_{is,Comp}$	87	%	[30]
Isentropic efficiency of pumps, $\eta_{is,Pump}$	87	%	[30]
Digestion temperature, $T_{Digestion}$	328	*K*	[30]
Combustion temperature, T_{CC}	1800	*K*	[30,31]
Organic Rankine Cycle (ORC)			
Isentropic efficiency of ORC turbines, $\eta_{is,Tur}$	89	%	[32]
ORC maximum pressure	4000	kPa	[32]
Isentropic efficiency of ORC pumps, $\eta_{is,Pump}$	87	%	[32]
Thermophotovoltaic (TPV)			
Energy band gap, E_g	1.1	*eV*	[33]
Surface area of emitter, A	0.045	m^2	[33]
Radiative emissivity of the emitter, ϵ_{em}	0.9	–	[33]
Diode ideality factor, Γ	1	–	[33]
Number of cells in TPV, Num_{cell}	185	–	–
Correction factor, β	0.96	–	[33]
Vanadium chloride (VCl)			
Cold end temperature difference of Sep1 in VCl, $CETD_{Sep1,VCl}$	125	*K*	–
Steps temperature	798, 573, and 373	*K*	[28]
Ammonia synthesis unit			
Ammonia synthesis reaction pressure	300	*bar*	[34]
Ammonia synthesis reaction temperature	673	*K*	[34]
Hydrogen to nitrogen molar ratio	3:1	–	[34]
Methanation unit			
Hydrogen to carbon dioxide molar ratio	4:1	–	[35]
Methanation reaction pressure	2500	*kPa*	[35]
Input data for economic analysis			
Plant expected life, *bl*	20	*year*	[30]
Annual number of hours, N	7000	*hour*	[30]
Maintenance factor, ϕ_r	1.06	–	[30]
Interest rate, i	15	%	[30]
LNG import price, $c_{LNG,in}$	6.982	$\$/GJ$	[36]
Digestion fuel price, $c_{biomass}$	11	$\$/GJ$	[37]
Ammonia price, c_{NH_3}	1.6	$\$/kg$	[38]
Methane price, c_{CH_4}	0.4	$\$$/kg	[39]
LNG selling price, $c_{LNG,out}$	1.15	$\$/GJ$	[40]
Electricity price, c_{elec}	0.14	$\$/kWh$	[30]

Table 3
Governing equations for mass, energy, and exergy balances in the system framework.

Mass balance	$\sum_{in}\dot{m} = \sum_{out}\dot{m}$
Energy balance	$\dot{Q} + \sum_{in}\dot{m}h = \sum_{out}\dot{m}h + \dot{W}$
Exergy balance	$\sum_{Inlets}\dot{E}_i + \sum\dot{Q}_j\left(1 - \frac{T_0}{T_j}\right) = \sum_{Outlets}\dot{E}_e + \dot{W}_{cv} + \dot{I}_{cv}$
Exergy	$\dot{E} = \dot{E}_{ph} + \dot{E}_{ch}$
Physical exergy	$\dot{E}_{ph} = \sum\dot{m}_i[(h_i - h_0) - T_0(s_i - s_0)]$
Chemical exergy	$\dot{E}_{ch} = \dot{n}\left(\sum y_i\overline{e}_i^{ch,0} + \overline{R}T_0\sum y_i\,ln(y_i)\right)$
Exergy efficiency	$\varepsilon_i = \frac{\dot{E}_P}{\dot{E}_F} = 1 - \frac{\dot{E}_D + \dot{E}_L}{\dot{E}_F}$

digestate. Due to the minimal generation of other gases during anaerobic digestion, their effects are considered insignificant and thus omitted from the analysis [29].

3.3. Ammonia synthesis unit

In the ammonia synthesis stage, hydrogen generated by the vanadium chloride unit and the input nitrogen are first compressed before being fed into the ammonia reactor, where they react to form pure ammonia. The formation of NH_3 is governed by a reversible chemical reaction, which can be represented by the following equation [44]:

$$N_2 + 3H_2 \rightarrow 2NH_3 \tag{2}$$

The foundational principles underlying the energy and exergy evaluation of the ammonia synthesis reactor are presented in the subsequent expressions [44]:

$$\eta_{en,ammonia\ synthesis\ unit} = \frac{(\dot{m}_{NH_3} \times h_{NH_3,product})}{(\dot{m}_{mix,in} \times h_{mix,in}) + \dot{W}_{comp,NH_3}} \tag{3}$$

$$\eta_{ex,ammonia\ synthesis\ unit} = \frac{\dot{E}x_{NH_3}}{\dot{E}x_{mix,in} + \dot{W}_{comp,NH_3}} \tag{4}$$

3.4. Vanadium-chloride cycle

The main steps and reactions of the VCl thermochemical cycle are presented below [45]:

$$2VCl_{3(s)} \rightarrow 2VCl_{2(s)} + Cl_{2(g)} \quad Temp = 798\ K\ (_{\text{Step 1}}) \tag{5}$$

$$Cl_{2(g)} + H_2O_{(g)} \rightarrow 2HCl_{(g)} + \frac{1}{2}O_{2(g)} \quad Temp = 373\ K\ (_{\text{Step 2}}) \tag{6}$$

$$2VCl_{2(s)} + 2HCl_{(g)} \rightarrow 2VCl_{3(s)} + H_{2(g)} \quad Temp = 573\ K\ (_{\text{Step 3}}) \tag{7}$$

To assess the efficiency and overall performance of the cycle, energy and exergy streams are methodically analyzed at every stage. The evaluation is conducted based on the core assumptions outlined in Ref. [28]. Under the premise of steady-state and steady-flow operation, conservation laws for mass, energy, and exergy are employed to determine thermal energy input, identify exergy losses, and evaluate the cycle's energy conversion effectiveness [19].

$$\bar{h}(T) - \bar{h}_0 = A(T) + B\left(\frac{T^2}{2}\right) + C\left(\frac{T^3}{3}\right) + D\left(\frac{T^4}{4}\right) - \frac{E}{T} + F - H \quad \left[\frac{kJ}{mole}\right] \tag{8}$$

$$\bar{s}(T) = A[\ln[T]] + B(T) + C\left(\frac{T^2}{2}\right) + D\left(\frac{T^3}{3}\right) - \frac{E}{(2T^2)} + G \quad \left[\frac{J}{mole,K}\right] \tag{9}$$

$$C_P(T) = A + B(T) + C(T^2) + D(T^3) + \frac{E}{T^2} \quad \left[\frac{J}{mole,K}\right] \tag{10}$$

The numerical values of the constants used in the previously mentioned equations are listed in Table 4.

Table 4 presents the thermodynamic constants for hydrogen and chlorine gases within the temperature range of 298–1000 K, as well as for hydrogen chloride gas from 298 to 1200 K. For vanadium dichloride (VCl_2) and vanadium trichloride (VCl_3), temperature-dependent enthalpy and specific heat capacities are determined using the empirical correlations outlined in Ref. [28], which describe the variation of these properties with temperature [28].

For VCl_2:

$$\bar{h}(T) - \bar{h}_0 = (17,25)T + (1,36 \times 10^{-3})T^2 + (0,71 \times 10^5)T^{-1} - 5502 \tag{11}$$

$$C_P(T) = (17,25) + (2,72 \times 10^{-3})T - (0,71 \times 10^5)T^2 \tag{12}$$

For VCl_3:

$$\bar{h}(T) - \bar{h}_0 = (22,99)T + (1,96 \times 10^{-3})T^2 + (1,68 \times 10^5)T^{-1} - 7592 \tag{13}$$

$$C_P(T) = (22,99) + (3,92 \times 10^{-3})T - (1,68 \times 10^5)T^2 \tag{14}$$

The valid temperature range for the equations spans from 298 to 1200 K for VCl_2 and from 298 to 900 K for VCl_3. It is important to highlight that enthalpy values are reported in cal/mol, whereas specific heat capacities are provided in cal/mol·K. The standard enthalpy of formation is −452.17 kJ/mol for VCl_2 and –581.13 kJ/mol for VCl_3. Their respective standard entropy values are 0.0493 kJ/mol·K for VCl_2 and 0.06462 kJ/mol·K for VCl_3 [28].

Furthermore, the chemical exergy values for the respective reactants and products, as provided in Ref. [46], are fundamental to the exergy evaluation of the thermochemical cycle.

3.5. Thermophotovoltaic unit

The thermophotovoltaic (TPV) system harnesses radiative heat emitted by the combustion chamber and transforms it into electrical energy using photovoltaic cells sensitive to infrared radiation. A high-temperature emitter absorbs the waste heat and re-radiates it, enabling its conversion by the PV cells. The overall efficiency of the TPV system is influenced by factors such as emitter temperature, spectral compatibility, and effective thermal regulation. A schematic representation of the TPV unit is provided in Fig. 2. Emitters are installed on the

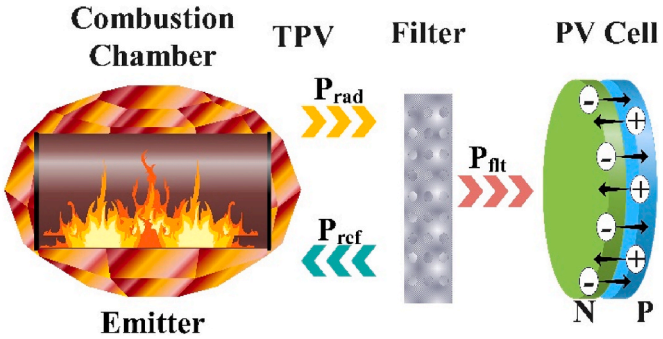

Fig. 2. The schematic of the TPV unit.

Table 4
Thermodynamic properties—formation enthalpy, standard entropy, and Shomate coefficients—of the VCl cycle compounds [19,28].

Compounds	$\bar{h}_f^0\left[\frac{kJ}{mole}\right]$	$\bar{s}_0\left[\frac{J}{mole,K}\right]$	A	B	C	D	E	F	G	H
$H_2O_{(g)}$	−241.83	188.84	−203.6	1523.29	−3196.4	2474.45	3.855	−265.55	−488.72	−285.83
$Cl_{2(g)}$	0	223.08	33.051	12.23	−12.065	4.385	−0.159	−10.834	259.03	0
$O_{2(g)}$	0	205.15	31.322	−20.235	57.866	−36.5	−0.007	−8.903	246.8	0
$H_{2(g)}$	0	130.68	33.066	−11.363	11.432	−2.772	−0.0158	−9.981	172.7	0
$HCl_{(g)}$	−92.31	186.9	32.124	−13.458	19.868	−6.854	−0.049	−101.62	228.68	−92.312

outer surfaces of the combustion chamber (CC) to enable the dissipation of surplus thermal energy into the environment.

The spectral intensity of blackbody emission, symbolized as I_b, is mathematically expressed by the equation below [47]:

$$I_b = \frac{2hc^2}{\lambda^5} \frac{1}{\exp\left[\frac{hc}{\lambda k T_{em}}\right] - 1} \tag{15}$$

Here, Planck's constant is denoted by h $= 6.626 \times 10^{-34}$(Js), the emitter temperature is T_{em} in Kelvin, wavelength λ is expressed in meters, the speed of light is c $= 2.997 \times 10^{8}(m/s)$, and Boltzmann's constant is given as k $= 1.381 \times 10^{-23}$(J/k) [47].

When radiative energy strikes the filter, only wavelengths shorter than a predefined limit are transmitted, while longer, lower-energy wavelengths are reflected back toward the emitter. In essence, radiation exceeding the cut-off wavelength does not reach the photovoltaic (PV) cells but is instead redirected to the emitter to support the maintenance of its elevated surface temperature. This wavelength threshold, referred to as the cut-off wavelength and represented by λcλc (in meters), is calculated using the following expression [33]:

$$\lambda_c = \frac{hc}{E_g} \tag{16}$$

The energy band gap of a photovoltaic cell, symbolized as E_g, is material-dependent. For cells made of silicon, E_g is about 1.1 eV, which aligns with a cut-off wavelength near 1.1 μm [33].

The fraction of radiative energy transmitted through the filter is calculated using the following equation, derived from the spectral distribution of radiation incident on each photovoltaic cell [33]:

$$P_{flt} = \varepsilon_{em} A \int_0^{\lambda_c} I_b\,(\lambda, T_{em}) d\lambda \tag{17}$$

In this context, A refers to the emitter's surface area measured in square meters (m^2), while ε_{em} indicates the radiative emissivity of the emitter, which depends on its material properties. For the purposes of this study, the emissivity is taken to be 0.9 [33].

The radiative energy that successfully passes through the filter is ultimately absorbed by the photovoltaic (PV) cells and converted into electrical energy [47]:

$$P_{el} = J_{sc} \times V_{oc} \times FF \times Num_{cell} \times A \tag{18}$$

Here, Num_{cell} represents the number of photovoltaic cells utilized in the thermophotovoltaic (TPV) module, and J_{sc} denotes the short-circuit current density, given in units of A/m^2 [33]:

$$J_{sc} = \int_{\lambda_{min}}^{\lambda_c} \frac{q_0 \lambda}{hc} EQE\,(\lambda) I_b\,(\lambda) d\lambda \tag{19}$$

Within this formula, the elementary charge is denoted as $q_0 = 1.602 \times 10^{-19}c$, and EQE corresponds to the external quantum efficiency of the PV cells, which is derived using Equation (20) and the input values outlined in Table 5 [33].

$$EQE = A + B\lambda + C\lambda^2 + D\lambda^3 + E\lambda^4 + F\lambda^5 \tag{20}$$

The parameter λ_{min} defines the minimum absorbable wavelength by the PV cell and is mathematically related to the cut-off wavelength through the expression below [33]:

$$\lambda_{min} = \frac{\lambda_c}{2.5} \tag{21}$$

The term V_{oc} refers to the open-circuit voltage, quantified in units of volts (V) [33]:

$$V_{oc} = \frac{\Gamma k T_c}{q_0} \ln\left[\frac{J_{sc}}{J_0} + 1\right] \tag{22}$$

Here, Γ represents the diode ideality factor and is assumed to have a value of 1 in this analysis. The photovoltaic cell temperature, T_c, is maintained at 300 K, and J_0, the saturation current density, is computed using the following relation [33]:

$$J_0 = 1.5 \times 10^5 \exp\left[\frac{-E_g}{kT_c}\right] \tag{23}$$

In this context, FF stands for the fill factor—a unitless metric that reflects the performance quality of a photovoltaic cell's output behavior [33]:

$$FF = \beta \frac{\nu - \ln[\nu + 0.71]}{\nu + 1} \tag{24}$$

Within this framework, β serves as the correction factor and is assigned a fixed value of 0.96 in this study. The parameter ν is calculated according to the following expression [33]:

$$\nu = \frac{q_0 V_{oc}}{kT_c} \tag{25}$$

3.6. Methanation unit

The conversion pathway of CO_2 to methane within the reactor system involves two sequential reactions: the first being the reverse water-gas shift (RWGS) reaction, detailed in Eq. (27), and the second, the methanation of CO, as illustrated in Eq. (28), all following the overall reaction in Eq. (26) [35,48–50]:

$$CO_2 + 4H_2 \leftrightarrow CH_4 + 2H_2O \Delta H_{298\,K} = -165 \left[\frac{kJ}{mol}\right] \tag{26}$$

$$CO_2 + H_2 \leftrightarrow CO + H_2O \Delta H_{298\,K} = +41,2 \left[\frac{kJ}{mol}\right] \tag{27}$$

$$CO + 3H_2 \leftrightarrow CH_4 + H_2O \Delta H_{298\,K} = -206,1 \left[\frac{kJ}{mol}\right] \tag{28}$$

The evaluation of the CO_2 methanation results is carried out through a mole balance applied to the complete reaction, employing stoichiometric ratios expressed in units of kilomoles [35]:

$$\nu_{CO_2} CO_2 + \nu_{H_2} H_2 + \nu_{CH_4} CH_4 + \nu_{H_2O} H_2O + \nu_{CO} CO \leftrightarrow \mu_{CO_2} CO_2 + \mu_{H_2} H_2 + \mu_{CH_4} CH_4 + \mu_{H_2O} H_2O + \mu_{CO} CO \tag{29}$$

The starting amounts of reactants are represented by ν_i, while μ_i

Table 5
Quantum efficiency (EQE) fitting equation [33].

λ	A	B	C
298 < λ < 652 nm	1.972520059E+3	−1.707929083E+1	5.464737856E-2
652 < λ < 1178 nm	−2.713351231E+4	1.609912944E+2	−3.768227025E-1
λ	D	E	F
298 < λ < 652 nm	−7.470290742E-5	3.726888675E-8	0
652 < λ < 1178 nm	4.362154125E-4	−2.495276528E-7	5.635111095E-11

indicates the molar quantities of the resulting products. To determine the final composition of the gaseous mixture, five primary unknown product values must be identified. This is accomplished by applying mole balance equations based on the conservation of carbon, hydrogen, and oxygen atoms (as outlined in Equations (30) and (31)), in conjunction with the equilibrium constraints of the reactions, described in Equations (32) and (33) [35]:

Carbon balance:

$$\nu_{CO_2} + \nu_{CH_4} + \nu_{CO} = \mu_{CO_2} + \mu_{CH_4} + \mu_{CO} \tag{30}$$

Hydrogen balance:

$$\nu_{H_2} + 2\nu_{CH_4} + \nu_{H_2O} = \mu_{H_2} + 2\mu_{CH_4} + \mu_{H_2O} \tag{31}$$

Oxygen balance:

$$\nu_{CO_2} + \frac{1}{2}\nu_{H_2O} + \frac{1}{2}\nu_{CO} = \mu_{CO_2} + \frac{1}{2}\mu_{H_2O} + \frac{1}{2}\mu_{CO} \tag{32}$$

Reverse water–gas shift:

$$Kp_{RWGS} = \frac{x_{CO}\cdot x_{H_2O}}{x_{CO_2}\cdot x_{H_2}} = \frac{\mu_{CO}\cdot \mu_{H_2O}}{\mu_{CO_2}\cdot \mu_{H_2}} \tag{33}$$

CO methanation:

$$\begin{aligned} Kp_{CO} &= \frac{x_{CH_4}\cdot x_{H_2O}}{x_{CO}\cdot x_{H_2}^3}\cdot\left(\frac{P_r}{P_a}\right)^{-2} \\ &= \frac{\mu_{CH_4}\cdot \mu_{H_2O}\cdot\left(\mu_{CO_2}+\mu_{H_2}+\mu_{CH_4}+\mu_{H_2O}+\mu_{CO}\right)^2}{\mu_{CO}\cdot \mu_{H_2}}\cdot\left(\frac{P_r}{P_a}\right)^{-2} \end{aligned} \tag{34}$$

The equilibrium constant for the *ith* reaction is denoted by Kp_i, and the associated molar fraction of each species x_i is determined on a wet basis. P_r represents the internal pressure of the reactor, whereas P_a corresponds to the surrounding or atmospheric pressure. The value of Kp_i is calculated using the expression given in Eq. (35), which serves as the foundation for the equilibrium analysis conducted in this study [35]:

$$Kp_i = e^{-\frac{G_i}{RT_r}} \tag{35}$$

Within this analysis, G_i denotes the change in Gibbs free energy associated with the ith reaction, as defined in Equations (36) and (37). The symbol T_r refers to the reactor's operational temperature. Notably, the Gibbs free energy for each chemical species is computed using the relation $g = h - T_r s$, as outlined in Equations (33) and (34) [35]:

$$G_{RWGS} = g_{H_2O} + g_{CO} - g_{H_2} - g_{CO_2} \tag{36}$$

$$G_{CO} = g_{CH_4} + g_{H_2O} - 3g_{H_2} - g_{CO} \tag{37}$$

The reactor temperature is estimated using an energy balance method, as outlined in Eq. (38). This evaluation accounts for the enthalpy variations linked to the reactions defined in Equations (26) and (27). A central assumption in this analysis is that the total heat generated by the exothermic reactions is fully utilized to increase the temperature of the products from their initial conditions to the final reaction temperature [35]:

$$\sum_i Cp_i\cdot\mu_i\cdot(T_r - T_{in}) = -\Delta H_{RWGS}\cdot\left(\nu_{CO_2} - \mu_{CO_2}\right) - \Delta H_{CO}\cdot\left(\nu_{CO_2} - \mu_{CO_2} - \mu_{CO}\right) \tag{38}$$

3.7. Techno-economic analysis and economic analysis

Evaluating the feasibility, economic effectiveness, and comparative cost-efficiency of energy systems relative to alternative technologies is a critical aspect of techno-economic analysis. The parameter $\dot{Z}$ represents the total financial investment associated with deploying the system, encompassing both initial capital costs and ongoing operation and maintenance expenses for all integrated components [41]:

$$\dot{Z}_k = Z_k^{CI} + Z_k^{OM} \tag{39}$$

The value of $\dot{Z}_k$ is estimated using the following equation, which is based on the available data for the purchase equipment cost (PEC) [41]:

$$\dot{Z}_k = Z_k^{CI} + Z_k^{OM} = CRF \times TCI_k \times \left(\frac{24\times 365}{N}\right) + \phi_r \times PEC_k \tag{40}$$

Within this expression, the capital recovery factor is symbolized by CRF, N indicates the total operational hours per year, bl represents the anticipated system lifetime, i is the yearly interest rate, and ϕ_r reflects the correction factor for maintenance and repair costs [41].

$$CRF = \frac{i(1+i)^n}{i(1+i)^n - 1} \tag{41}$$

To ensure cost accuracy, the final step involved updating equipment purchase prices to present-day figures through the application of the Chemical Engineering Plant Cost Index (CEPCI) [41]:

$$PEC_k = PEC \times \frac{CEPCI_{2022}}{CEPCI_{orginal}} \tag{42}$$

The cost index for 2022 is 813 [51].

The overall expense rate attributed to the multi-generation system is represented through the subsequent expression [52]:

$$\dot{Z}_{tot} = \sum \dot{Z}_k \tag{43}$$

A component-level economic analysis of the system is provided in Table S.1 of the Supplementary file.

As shown in Table 6, the Total Capital Investment (TCI) for the proposed power system is determined through the integration of multiple cost factors. This evaluation accounts for both direct and indirect fixed costs, with specific exclusions applied where appropriate. Together, these categorized expenses form the foundation for estimating the overall capital investment [41]:

$$TCI = FCI + other\ outlays = DC + IC \tag{44}$$

Before committing financial resources, it is crucial to assess the expected return on investment. The Net Present Value (NPV) method is used to evaluate the economic viability of the proposed system by discounting future annual net cash flows to their present value using the prevailing interest rate, thus providing a clear picture of its long-term profitability [41]:

$$NPV_{bl} = -TCI + \sum_{bl=0}^{bl} Y\ IF_{bl}\ RDF_{bl} \tag{45}$$

For the purpose of this analysis, i denotes the assumed interest rate of 15 %, and bl signifies the estimated economic lifetime of the system, taken as 20 years. The term Y represents the net cash flow at the end of the system's final year of operation and is calculated through the

Table 6
Elements of the total capital investment [41].

Total Capital Investment (TCI)	Direct cost (DC)	Onsite costs (ONSC)	Purchased − equipment cost (PEC) Purchased − equipment installation (PEI) = 0.33 × PEC Piping = 0.35 × PEC Electrical equipment and materials = 0.13 × PEC
		Offsite costs (OFSC)	Land = 0.05 × PEC Civil, structural, and architectural work = 0.21 × PEC Service facilities = 0.35 × PEC
	Indirect cost (IC)		Engineering and supervision = 0.08 × DC Construction costs, including contractor's profit = 0.15 × DC Contingencies = 0.15 × (1.23 × DC)

subsequent expression [30,41]:

$$Y = AI - \left(C^{O\&M} + C_f\right) \tag{46}$$

The variable AI represents the system's annual income, while $C^{O\&M}$ denotes the costs associated with operation and maintenance. Fuel-related expenditures are indicated by C_f. A comprehensive description of these parameters is provided in the following section [30,41]:

$$AI = c_{elec} \times N \times \dot{W}_{net} + c_{LNG,out} \times N \times \dot{E}_{LNG,out} \times 0,0036 + c_{CH_4} \times N \times \dot{m}_{CH_4} \times 3600 + c_{NH_3} \times N \times \dot{m}_{NH_3} \times 3600 + c_{N_2} \times N \times \dot{m}_{N_2} \times 3600 \tag{47}$$

$$C^{O\&M} = 0,06 \times PEC \tag{48}$$

$$C_f = \dot{C}_{biomass} + \dot{C}_{LNG,in} \tag{49}$$

$$IF_{bl} = \left(1 + \left(\frac{i}{100}\right)\right)^{-bl} \tag{50}$$

$$RDF_{bl} = \left(1 + \left(\frac{Ri}{100}\right)\right)^{-bl} \tag{51}$$

The Payback Period (PBP) is defined as the duration required for the Net Present Value (NPV) to turn positive, signifying full recovery of the initial investment. In the context of the reference system, the PBP indicates the timeframe within which the accumulated NPV surpasses zero, denoting the onset of profitability [41].

$$PBP = min\{bl : NPV(bl) > 0\} \tag{52}$$

3.8. Environmental analysis

In this work, the environmental assessment is carried out in a simplified manner and serves mainly as a comparative tool within the parametric analysis. Its purpose is to provide a preliminary insight into how different design variables affect the system's environmental performance. While this qualitative approach helps highlight major sources of environmental impact, it does not encompass a comprehensive accounting of emissions or resource consumption [53].

$$\zeta = \frac{3600 \times \dot{m}_{CO_2}}{\dot{m}_{CH_4} \times LHV_{CH_4} + \dot{m}_{NH_3} \times LHV_{NH_3} + \dot{W}_{net,Total}} \tag{53}$$

3.9. Performance criteria

The exergy efficiency of the system is assessed based on the equation provided below:

$$\left(\eta_{exergy}\right)_{total} = \frac{\dot{W}_{net,Total} + \dot{E}_{CH_4} + \dot{E}_{NH_3} + \dot{E}_{LNG,out}}{\dot{E}_{biomass} + \dot{E}_{LNG,in}} \tag{54}$$

The specific production cost associated with the multi-generation system is determined through the following expression:

$$C_{p,total} = \frac{\dot{C}_{biomass} + \dot{C}_{LNG,in} + \dot{Z}_{tot}}{\dot{W}_{net,Total} + \dot{E}_{CH_4} + \dot{E}_{NH_3} + \dot{E}_{LNG,out}} \tag{55}$$

3.10. Multi-objective optimization

The Gray Wolf Optimization (GWO) algorithm, introduced by Mir Jalali et al. [54] in 2014, is inspired by the social structure and cooperative hunting tactics of gray wolves. This biologically inspired technique is designed to tackle complex optimization problems by emulating the hierarchical roles and group behavior within a wolf pack. Compared to other metaheuristic algorithms such as Genetic Algorithm (GA), Particle Swarm Optimization (PSO), and Ant Colony Optimization (ACO), the Gray Wolf Optimizer (GWO) offers several distinct advantages that make it highly suitable for complex energy system optimization. GWO achieves an effective balance between exploration and exploitation through its nature-inspired hunting behavior, including tracking, encircling, and attacking the prey, which helps avoid premature convergence and improves the probability of reaching global optima. Additionally, GWO requires fewer control parameters—primarily the number of search agents and the adaptive coefficient 'a'—which simplifies implementation and tuning compared to algorithms like GA and PSO that demand calibration of multiple variables. Another advantage of GWO lies in its faster convergence speed toward optimal or near-optimal solutions, especially in nonlinear, multi-modal, and constrained environments such as thermal and hybrid energy cycles. Furthermore, GWO demonstrates strong performance in handling high-dimensional and multi-objective problems, making it well-suited for applications involving simultaneous optimization of energy, exergy, economic, and environmental criteria [54]. In multi-objective applications, the algorithm is enhanced through the use of Pareto dominance theory to ensure both solution diversity and convergence toward optimal trade-offs. Each potential solution is treated as a virtual wolf, assessed via an objective vector representing its performance across multiple criteria. Solutions are ranked according to dominance levels, with the most competitive, non-dominated individuals forming the leading Pareto front. The direction of the search is guided by the top three alpha wolves, who coordinate the movement of the rest of the population, reflecting the collaborative strategy used to locate the global optimum [54,55]:

$$\vec{D}_{\alpha} = \left|\vec{C}_1 \cdot \vec{X}_{\alpha}(t) - \vec{X}\right| \tag{56}$$

$$\vec{D}_{\beta} = \left|\vec{C}_2 \cdot \vec{X}_{\beta}(t) - \vec{X}\right| \tag{57}$$

$$\vec{D}_{\delta} = \left|\vec{C}_3 \cdot \vec{X}_{\delta}(t) - \vec{X}\right| \tag{58}$$

$$\vec{X}_1 = \vec{X}_{\alpha} - \vec{A}_1 \cdot \vec{D}_{\alpha} \tag{59}$$

$$\vec{X}_2 = \vec{X}_{\beta} - \vec{A}_2 \cdot \vec{D}_{\beta} \tag{60}$$

$$\vec{X}_3 = \vec{X}_{\delta} - \vec{A}_3 \cdot \vec{D}_{\delta} \tag{61}$$

$$\vec{X}(t+1) = \left(\vec{X}_1 + \vec{X}_2 + \vec{X}_3\right) \Big/ 3 \tag{62}$$

In this context, t denotes the current iteration number, $\vec{X}$ represents the position vector of a gray wolf, and $\vec{A}$ and $\vec{C}$ are the associated coefficient vectors.

An external Pareto archive is employed to retain the top-performing non-dominated solutions identified during the optimization process. The selection of the leading wolves—α, β, and δ—is guided by a strategic criterion focused on maximizing solution quality. To promote a well-distributed set of solutions along the Pareto front, the crowding distance method is implemented, supporting diversity preservation throughout the search space.

This study explores three distinct scenarios for multi-objective optimization, each designed to investigate specific trade-offs between economic, environmental, and production goals.

The first scenario focuses on minimizing the environmental index while still minimizing the total unit cost and improving second-law efficiency. This setting favors environmentally driven operation by reducing CO_2-equivalent emissions, even if it slightly compromises total fuel output. Here, the hydrogen split between methanation and ammonia synthesis is adjusted to favor the pathway that results in the lowest environmental impact under given operating conditions.

In the second scenario, the aim is to minimize total product cost, maximize methane production, and reduce the environmental index. Methane is prioritized in this case due to its role as a direct substitute for natural gas in existing infrastructure, making it a valuable target for regions with high gas demand. The trade-off is that ammonia output may be reduced to allocate more hydrogen toward methanation.

In the third scenario, the objectives are to minimize the total unit cost of the product, maximize the mass flow rate of ammonia, and improve second-law efficiency. This configuration prioritizes ammonia production because of its higher market value and strategic importance as both a fuel and an energy carrier. The trade-off in this case is a potential reduction in methane output, which is accepted in favor of maximizing ammonia's economic and storage advantages.

Implementation of the Multi-Objective Gray Wolf Optimization (MOGWO) technique involves specifying a set of decision variables (Table 7), which define operational boundaries and influence the optimization outcomes. These include oxygen liquefaction pressure, inlet temperature of the ORC turbine, hydrogen allocation ratio between methanation and ammonia synthesis, and outlet temperature of the combustion chamber.

Fig. 3 illustrates the study's methodology using a structured flowchart. The process initiates with an integrated evaluation of the multi-generation system, encompassing energy and exergy analyses alongside environmental and techno-economic assessments. This thorough investigation forms the basis for the optimization stage, where MATLAB is employed to enhance the system's overall efficiency and performance.

4. Validation

Validation of the ammonia synthesis subsystem was carried out using data from Magnino et al. [34] under steady-pressure conditions, with temperature results showing strong consistency, as presented in Table 8. Thermodynamic analysis was conducted in EES, while temperature distribution within the reactor was verified using CHEMKIN in Ansys. The minimal deviation from benchmark values confirms the reliability and precision of the developed model.

The methanation module was validated using reference data from Bailera et al. [35] under steady-pressure conditions. A comparison of temperature and mass flow rate values, as shown in Table 9, reveals close alignment with the reported data, affirming the model's accuracy in representing both thermal dynamics and flow characteristics.

Validation of the vanadium chloride cycle was conducted using heat demand data from Balta et al. [28], assuming isothermal reaction conditions. As presented in Table 10, the computed results exhibit strong agreement with the reference values, confirming both the model's precision and the credibility of the thermochemical hydrogen production route.

Validation of the TPV subsystem was performed by comparing simulation results with the numerical findings reported by Shun et al. [33], specifically examining the influence of oxygen consumption in the combustion chamber. As shown in Figs. 4 and 5, the predicted emitter temperature and power output for an individual TPV cell are closely aligned with the reference data, demonstrating the accuracy and credibility of the subsystem within the overall hybrid configuration.

Table 7
The broad spectrum of decision variables integrated into the Gray Wolf Optimization (GWO) framework.

Decision variable	Unit	Lower bound	Upper bound
Oxygen liquefaction pressure, P_{liq,O_2}	*kPa*	5000	5500
Inlet temperature of ORC turbine, $T_{ORC,turbine}$	*K*	480	520
Hydrogen ratio for methanation and ammonia synthesis unit, *ratio*	–	0.1	0.9
Outlet temperature of combustion chamber, T_{CC}	*K*	1700	1800

The Organic Rankine Cycle (ORC) model was verified by examining how variations in turbine inlet pressure influence energy efficiency. A comparison between the current study's results and those reported by Meng et al. [32] is illustrated in Fig. 6. The close correlation between the two datasets validates the accuracy and reliability of the ORC model applied in this research.

5. Results and discussion

5.1. Base mode results

In the base case scenario, the overall exergy efficiency of the hybrid system is calculated to be 38.45 %, based on the total exergy input and useful outputs. The exergy inputs consist of 31,523 kW from biomass and 6,112 kW from LNG, summing to a total exergy fuel input of 37,635 kW. The useful exergy outputs are 3,804 kW of electricity, 5,614 kW attributed to ammonia production, and 5,055 kW from methane synthesis. Based on these outputs and inputs, the calculated unit cost of the products is 36.27 $/GJ, indicating the system's economic viability under current assumptions. Furthermore, if the carbon dioxide produced were not captured, the resulting emission index would be 0.0692 kg/kWh, which highlights the environmental significance of integrating carbon capture technologies in such systems. The corresponding base-case decision variables are $P_{liq,O2} = 5000$ kPa, $T_{ORC,\ turb} = 500$ K, $T_{CC} = 1800$ K, and hydrogen split ratio = 0.5. The base-case production rates are 0.2769 kg/s (NH3) and 0.101 kg/s (CH4). The detailed thermodynamic properties of the system and the gas compositions of the subsystems are presented in Tables S2, S3, S4, and S5 of the Supplementary File.

Of the three subsystems utilizing waste energy streams, the VCl thermochemical cycle demonstrates the highest raw energy efficiency at 73.85 %, effectively converting high-temperature exhaust heat into chemical energy. The LNG cold energy recovery sub-system operates at a significantly efficient 42.87 %, while the Organic Rankine Cycle has the lowest pre-optimization energy efficiency at 22.1 %. Despite the varying performance of these individual components, the overall system integrates them effectively to achieve a total energy efficiency of 55.97 % before optimization. The total power generated is 3716 kW, consisting of 1258 kW from the ORC, 1789 kW from LNG heat recovery, and the remainder from the oxy-fuel gas cycle.

To highlight the competitiveness of the proposed configuration, a comparison with state-of-the-art systems reported in the literature is presented in Table 11. As shown, while some studies such as [8,9] report higher energy and exergy efficiencies (up to 84 % and 94.4 %), these systems are comprised of different components and subcycles and are associated with significantly higher product costs (e.g., 850 $/ton and 294.37 €/ton). In contrast, the present work achieves overall energy and exergy efficiencies of 55.97 % and 38.19 %, respectively, while maintaining a competitive total product cost of 36.6 $/GJ. Moreover, unlike most other works that focus on a limited range of products (e.g., methanol or hydrogen), the proposed system simultaneously delivers power, methane, and ammonia, offering greater operational flexibility and economic sustainability. This balance between thermodynamic performance, economic feasibility, and multi-product generation emphasizes the novelty and practical potential of the developed configuration.

5.2. Parametric study

To investigate the operational flexibility of the proposed system, a comprehensive parametric analysis was performed by varying key input parameters affecting the thermodynamic and economic performance. The studied parameters include the combustion chamber flame temperature, the final pressure of the oxygen compression stage for cryogenic separation, the ORC turbine inlet temperature, and the hydrogen allocation ratio between the methanation and ammonia synthesis units. Each parameter was independently varied within a defined range while

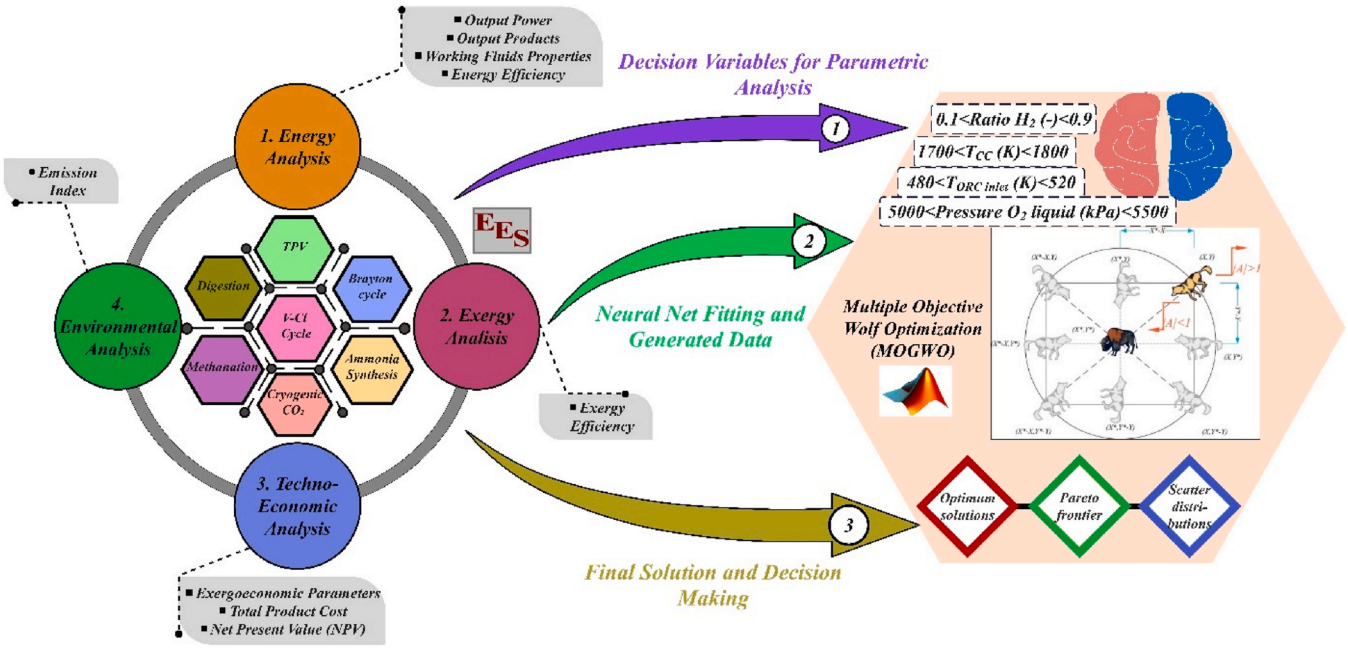

Fig. 3. The flowchart for modeling the system.

Table 8
Validation of ammonia synthesis unit.

Stream	Pressure [bar]	Temperature [°C] of Magnino et al. [34]	Temperature [°C] of the present work (EES software)	Error [%]	Temperature [°C] of the present work (CHEMKIN software)	Error [%]
1	300	25	25	0	–	–
2	300	25	25	0	–	–
3	300	194.2	196.5	1.18	–	–
4	300	400	400	0	–	–
5	300	583.5	578.3	0.89	573.5	1.71
6	299.5	400	400	0	–	–
7	299.5	507.6	509.6	0.39	503.9	0.72
8	299	400	400	0	–	–
9	299	476.1	473	0.65	468.9	1.51
10	298	30	30	0	–	–
11	298	30	30	0	–	–
12	297	11.5	11.5	0	–	–
13	297	11.5	11.5	0	–	–
14	300	12.6	12.52	0.63	–	–
15	300	309.5	312	0.8	–	–
16	297	11.5	11.5	0	–	–
17	298	30	30	0	–	–
18	30	29.5	29.5	0	–	–
19	30	29.5	29.5	0	–	–
20	20	29	29	0	–	–
21	20	29	29	0	–	–

monitoring the system's exergetic efficiency, net power output, product cost, and environmental index to assess their individual and collective impacts on system behavior.

Fig. 7 illustrates the effect of varying the outlet temperature of the combustion chambers from 1700 K to 1800 K on the system's thermodynamic, economic, and environmental performance indicators. As the outlet temperature increases within this range, several significant trends are observed.

The exergy efficiency (η_{exergy}) improves gradually from approximately 38.17 % at 1700 K to about 38.48 % at 1800 K. This enhancement is attributed to improved gas turbine performance and higher thermal energy availability for the VCl thermochemical hydrogen production and ORC subsystems at elevated combustion temperatures. Higher combustion temperatures increase the specific work output and enhance the effective utilization of exhaust heat, thereby improving the overall system exergy performance.

The methane production rate ($\dot{M}\ C_{H4}$) rises steadily from around 0.098 kg/s at 1700 K to 0.101 kg/s at 1800 K. Simultaneously, the ammonia production rate ($\dot{M}\ N_{H3}$) increases from 0.268 kg/s to 0.277 kg/s across the same temperature range. The higher exhaust gas temperatures provide additional thermal energy to the VCl cycle, boosting hydrogen production. This increased hydrogen availability directly enhances the synthesis rates of both methane, through methanation with captured CO_2, and ammonia, via reaction with separated nitrogen. These upward trends in fuel synthesis confirm the positive impact of higher combustion temperatures on the chemical productivity of the system.

The total product cost (C_{ptotal}) exhibits a mild increase from 0.11 $/kWh at 1700 K to 0.114 $/kWh at around 1740 K, after which it rises more sharply, reaching 0.132 $/kWh at 1800 K. This behavior can be attributed to the higher capital and operational costs associated with

Table 9
Validation of the methanation unit.

State	Pressure [bar]	Temperature [°C] of the present work	Temperature [°C] of ref. [35]	Error [%]	Mass flow rate [kg/s] of the present work	Mass flow rate [kg/s] of ref. [35]	Error [%]
1	25	308.6	308.6	0	7.2	7.2	0
2	25	333.2	333.2	0	1.3	1.319	1.44
3	25	597	591.6	0.9	38.5	38.72	0.56
4	25	300	300	0	38.5	38.72	0.56
5	25	300	300	0	30.1	30.21	0.36
6	25	300	300	0	8.5	8.519	0.22
7	25	463.5	460.5	0.64	8.5	8.519	0.22
8	25	197.4	197.4	0	4.9	4.911	0.22
9	25	197.4	197.4	0	3.5	3.609	3.02
10	25	300	300	0	3.5	3.609	3.02
11	25	352.3	354.4	0.59	16	16.4	2.43
12	25	300	300	0	16	16.4	2.43
13	25	300	300	0	12.5	12.8	2.34
14	25	300	300	0	3.5	3.609	3.02
15	25	155.7	155.7	0	2.7	2.679	0.78
16	25	155.7	155.7	0	0.9	0.9297	2.97

Table 10
Validation of vanadium chloride thermochemical cycle.

Step number	Step temperature [K]	Reaction heat demand [kJ/mole H_2]		
		Balta et al. [28]	Present work	Error [%]
1	798	349.6	348.97	0.18
2	373	70.77	70.33	0.62
3	573	−88.72	−87.99	0.82

equipment functioning at elevated temperatures, increased cooling demands, and greater water injection rates necessary for temperature regulation. Additionally, higher thermal loads increase auxiliary energy consumption and impose greater operational and maintenance demands, contributing to the escalating product cost, particularly beyond 1760 K. In contrast, the environmental impact index (ζ_{env}) decreases steadily from 0.072 kg/kWh at 1700 K to 0.0692 kg/kWh at 1800 K. This trend signifies an overall environmental performance improvement, driven by higher hydrogen, methane, and ammonia yields per unit of fuel input, alongside more efficient CO_2 capture and utilization. The reduced environmental index at higher temperatures results from improved resource conversion efficiencies and minimized waste emissions per unit of produced energy and fuel.

Fig. 8 presents the influence of varying the oxygen liquefaction pressure in the final compression stage from 5000 kPa to 5500 kPa on the thermodynamic, techno-economic, and environmental performance indicators of the system. The results show that changes in this parameter notably affect both the system's energy performance and product yields.

The exergy efficiency exhibits a consistent decline as the oxygen liquefaction pressure increases, decreasing from approximately 38.47 % at 5000 kPa to 37.88 % at 5500 kPa. This reduction is primarily due to the increasing power consumption associated with compressing air to higher pressures before cryogenic separation. The additional

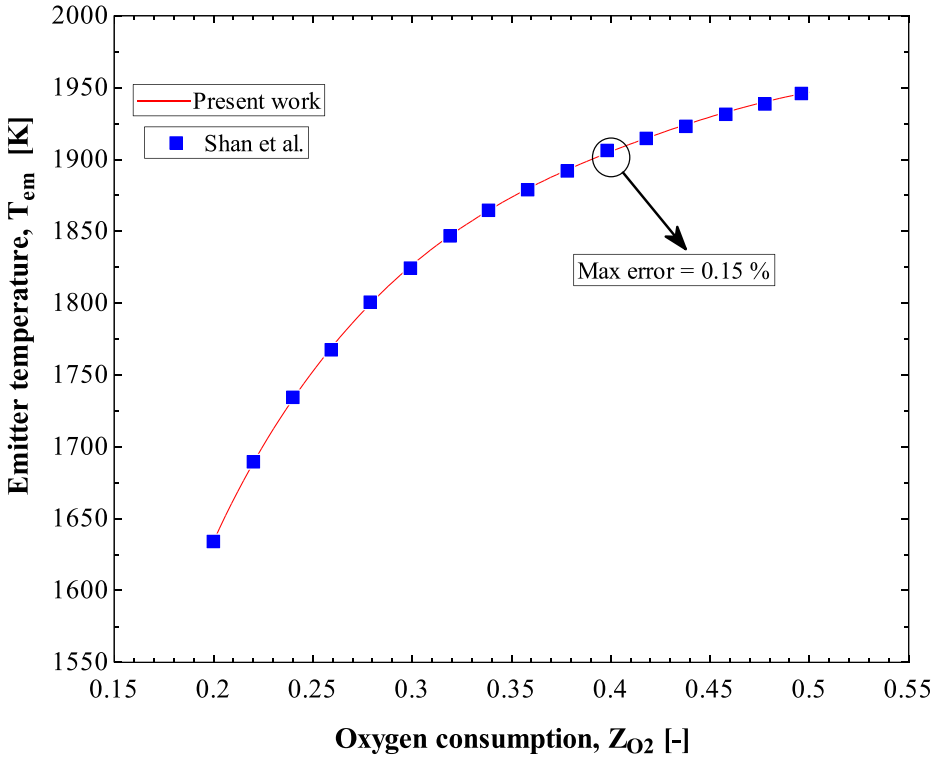

Fig. 4. Validation of thermophotovoltaic for the emitter temperature.

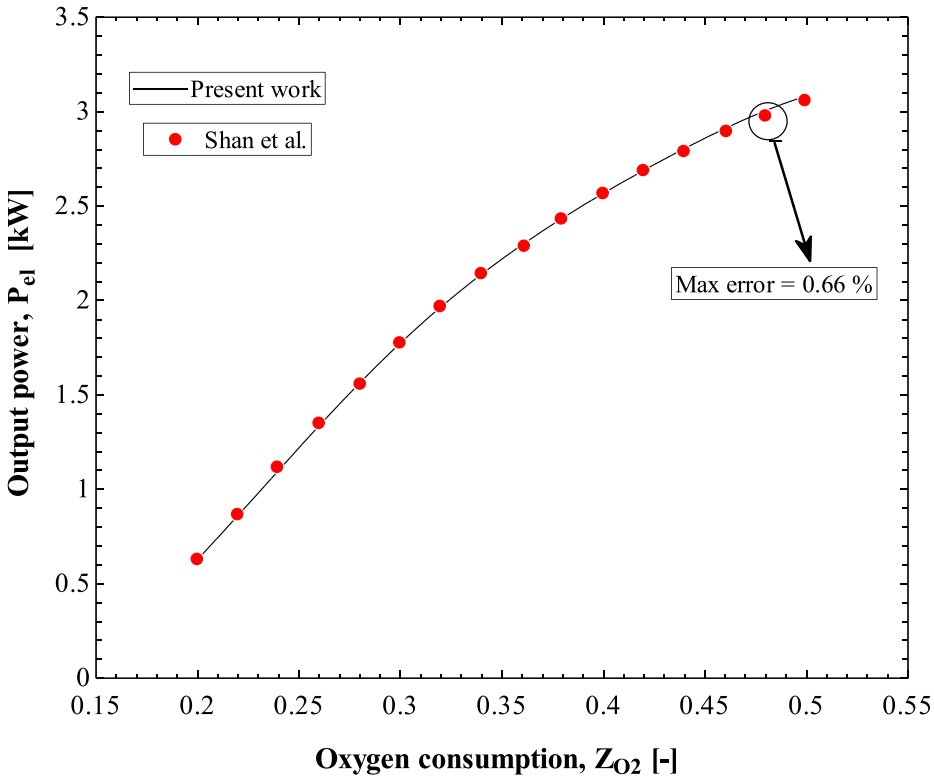

Fig. 5. Validation of thermophotovoltaic for the output power.

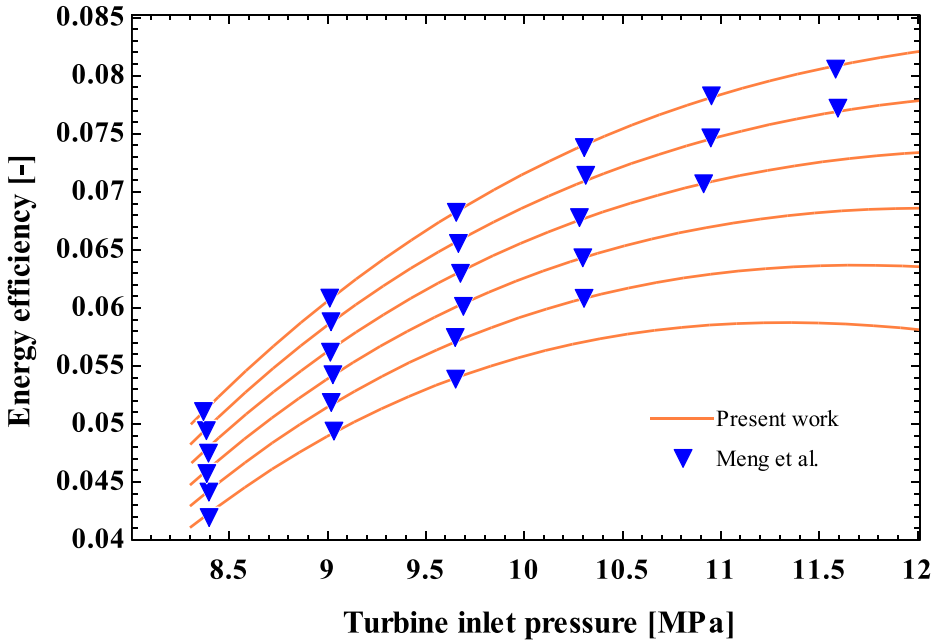

Fig. 6. Validation of organic Rankine Cycle.

compression work reduces the net power output of the system, thereby lowering the overall exergy efficiency.

The methane production rate follows a similar downward trend, dropping from about 0.1010 kg/s at 5000 kPa to 0.10075 kg/s at 5500 kPa. The decrease occurs because the higher compression work reduces the amount of useful heat and hydrogen available downstream for methanation after expansion at higher pressure rates. Likewise, the ammonia production rate decreases slightly from 0.2768 kg/s to 0.2765 kg/s over the same pressure range, driven by the diminished hydrogen production in the VCl cycle, which is thermally supported by the exhaust heat from the gas turbines. As the available heat decreases, the hydrogen generation rate drops, subsequently reducing both methane and ammonia synthesis rates.

Conversely, the total product cost rises steadily with increasing oxygen liquefaction pressure, moving from 0.1301 $/kWh at 5000 kPa to 0.1327 $/kWh at 5500 kPa. This trend is explained by the higher specific energy consumption of the air compression and liquefaction process at elevated pressures, which directly increases operational costs. As more

Table 11
Comparison of base case and state-of-the-art systems reported in the literature.

Ref.	Sub-systems	Products	Methodology	Thermodynamic results	Economic results
Present work	Oxyfuel gas turbine, Cryogenic air separation, TPV, LNG cold energy recovery, methanation, and ammonia synthesis	Power, methane, and Ammonia	Thermodynamics, Exergy, Techno-economics	Overall energy and exergy efficiency of 55.97 % and 38.19 %	Total cost of products: 36.6 $/GJ
[7]	EFGT, RC, ORC, MCFC, PEME, methanation, and methanol synthesis unit	Power, methane, and methanol	Exergy, and exergoeconomic	Overall energy efficiency of 41.8 %	Methane and methanol price of 79.4 and 92.8 $/MWh, respectively
[8]	Wind turbine, Electrolyzer, Biogas upgrading, Oxyfuel gas turbine, LNG cold energy recovery, Water gas shift reactor, Flue gas recycling	Power, Biofuel	Life cycle assessment, Techno-economics, Exergy	Overall energy and exergy efficiency of 84 % and 94.4 %	Levelized cost of fuels, 850 $/ton
[9]	Biogas-to-MeOH, SOEC, CCS	Hydrogen, Methanol	Thermodynamics, Techno-economic analysis, Life cycle assessment	Energy efficiency of 58.09 %	Levelized cost of fuels, 294.37 €/ton

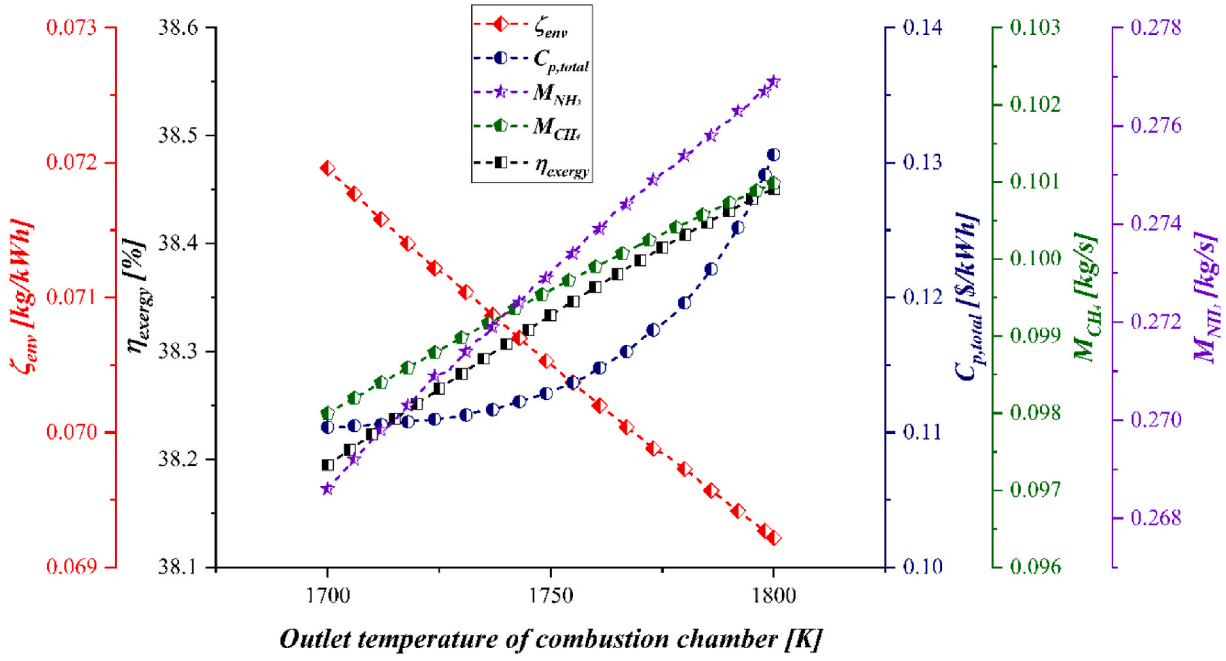

Fig. 7. Variation of combustion chamber temperature vs the key parameters.

energy is consumed in producing liquefied oxygen, less net power remains available for export, raising the unit cost of the produced energy and fuels. The environmental impact index also displays a mild but consistent upward trend, increasing from 0.0692 kg/kWh at 5000 kPa to 0.0698 kg/kWh at 5500 kPa. The environmental performance deteriorates slightly with increasing pressure due to reduced hydrogen, methane, and ammonia production efficiencies. These factors collectively result in a higher environmental index per unit of useful output.

Although this figure proves that the higher pressure for O_2 liquefication is thermodynamically and economically ineffective, the importance of increasing the O_2 liquefaction temperature via pressurizing the air should not be overlooked.

Fig. 9 illustrates the effect of the ORC turbine inlet temperature on key system performance indicators, including the exergy efficiency, total product unit cost, environmental impact factor, and the production rates of methane and ammonia. The turbine inlet temperature was varied from 480 K to 520 K to evaluate its influence on system behavior.

As seen in Fig. 9, the exergy efficiency shows a steady increase with rising turbine inlet temperature, improving from 38.435 % at 480 K to 38.465 % at 520 K. This enhancement results from the increased power recovery within the ORC cycle as higher temperatures raise the available thermal energy for conversion into mechanical work. In parallel, the environmental impact factor decreases from 0.06923 kg/kWh at 480 K to 0.069215 kg/kWh at 520 K, indicating a reduction in CO_2 emissions per unit of exergy produced as the ORC contributes more effectively to overall energy recovery.

The total product unit cost almost stays consistent at 0.1306 $/kWh, given the fact that the capital cost of the ORC turbine doesn't change dramatically with the narrow temperature range studied in this figure. Also, the production rates of methane and ammonia remain essentially constant throughout the studied temperature interval. The methane production rate holds steady at approximately 0.101 kg/s, while the ammonia production rate consistently remains near 0.277 kg/s. This outcome is expected since the ORC turbine inlet temperature predominantly affects the power recovery side of the system rather than the thermochemical reaction pathways for fuel synthesis.

Fig. 10 illustrates the influence of the hydrogen distribution ratio between the methanation and ammonia synthesis units on the system's key performance parameters, namely the exergy efficiency, environmental impact factor, total product unit cost, and the production rates of methane and ammonia. The hydrogen ratio — defined as the fraction of hydrogen sent to the methanation unit — was varied from 0.1 to 1.0, thereby shifting the entire hydrogen flow between the two downstream synthesis processes.

As depicted in the figure, increasing the hydrogen allocation to methanation significantly enhances the methane production rate, rising linearly from 0.02 kg/s at a ratio of 0.1 to approximately 0.19 kg/s at a ratio of 0.9. Conversely, the ammonia production rate drops in direct

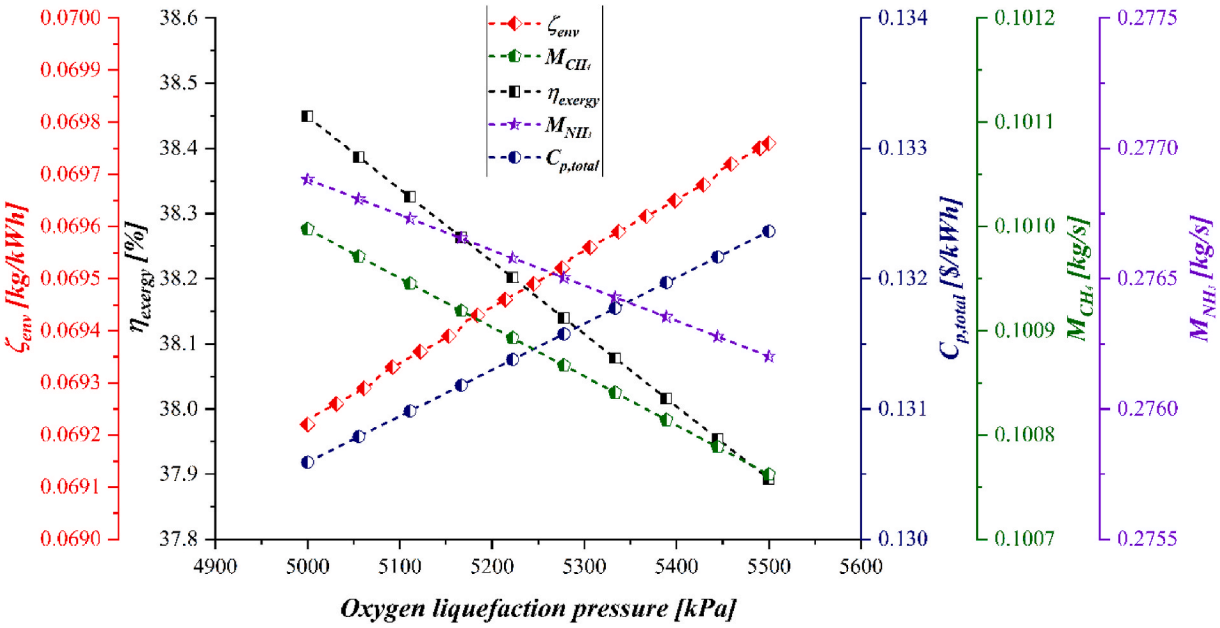

Fig. 8. Variation of Oxygen liquefaction pressure vs the key parameters.

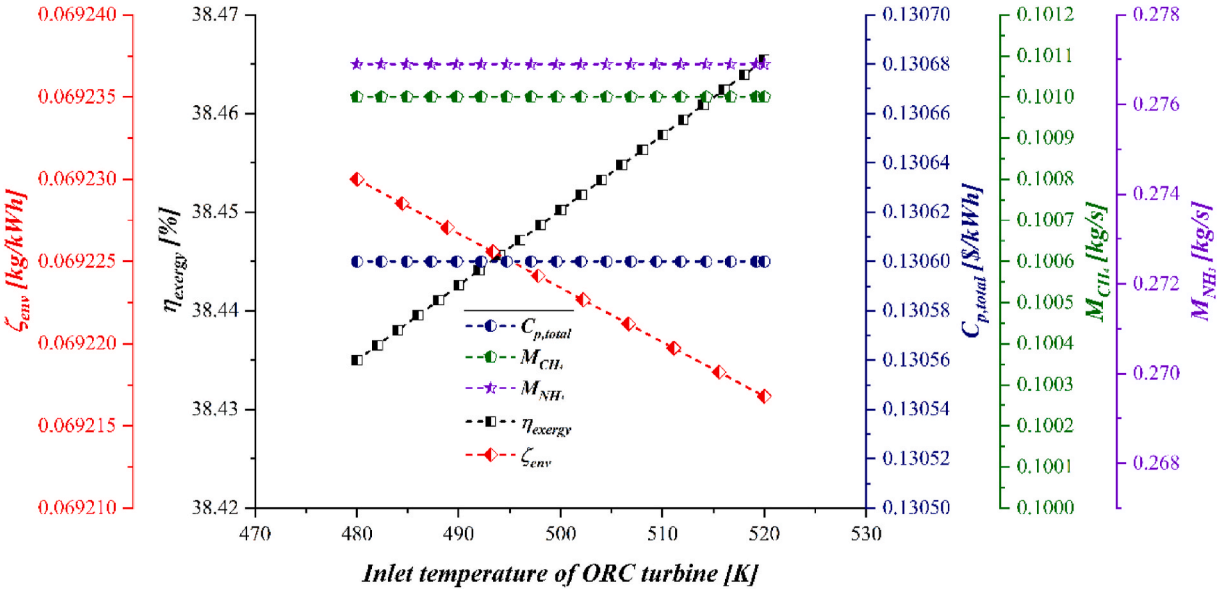

Fig. 9. Variation of Oxygen liquefaction pressure vs the key parameters.

proportion, decreasing from about 0.5 kg/s to 0.05 kg/s over the same range. This direct trade-off reflects the competitive nature of hydrogen use within the system.

The exergy efficiency exhibits a gradual decline from 39.75 % at a hydrogen ratio of 0.1–37.2 % at a ratio of 0.9. This reduction is attributed to the thermodynamic characteristics of the methanation process, which operates at lower thermal efficiencies compared to the ammonia synthesis pathway, thereby reducing the overall system exergy performance as more hydrogen is diverted toward methane production.

In parallel, the environmental impact factor increases from 0.0666 kg/kWh to 0.0716 kg/kWh as the hydrogen ratio shifts to methanation, driven by the higher CO_2 emissions associated with methane synthesis and the decrease in exergy efficiency. Likewise, the total product unit cost increases from 0.127 $/kWh to 0.135 $/kWh as hydrogen is redirected to methanation. This is due to the comparatively lower market value of methane relative to ammonia and the associated economic penalties of producing a larger share of lower-value fuel.

5.3. Economic evaluation (NPV)

In Fig. 11, the net present value (NPV) of the integrated system is evaluated over a 20-year project lifetime while varying the selling price of ammonia (C_{nh3}) at 1.2, 1.4, and 1.6 $/kg. The other product prices are held constant at 0.02 $/kg for nitrogen, 0.4 $/kg for methane, 0.14 $/kWh for electricity, and 1.15 $/GJ for LNG. The NPV trajectory starts from a negative value of around −58 M$ due to the high initial investment (capital and lifetime operation costs summing to approximately 73.8 M$) and increases over time as revenues accumulate from product sales. As expected, higher ammonia prices significantly improve the economic performance of the system. At C_{nh3} = 1.6 $/kg, the payback period is reached earliest at 4.5 years, followed by 5.01 years for 1.4 $/kg, and 5.71 years for 1.2 $/kg. After 20 years, the final NPV at C_{nh3} =

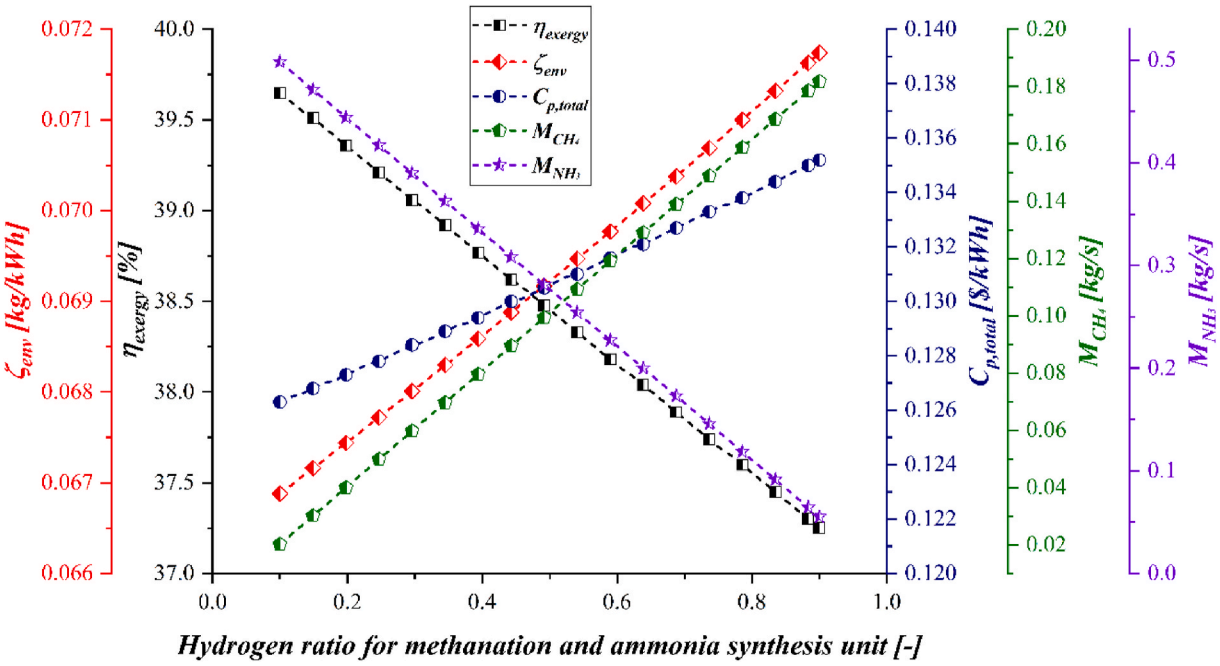

Fig. 10. Variation of the hydrogen distribution ratio between the methanation and ammonia synthesis units.

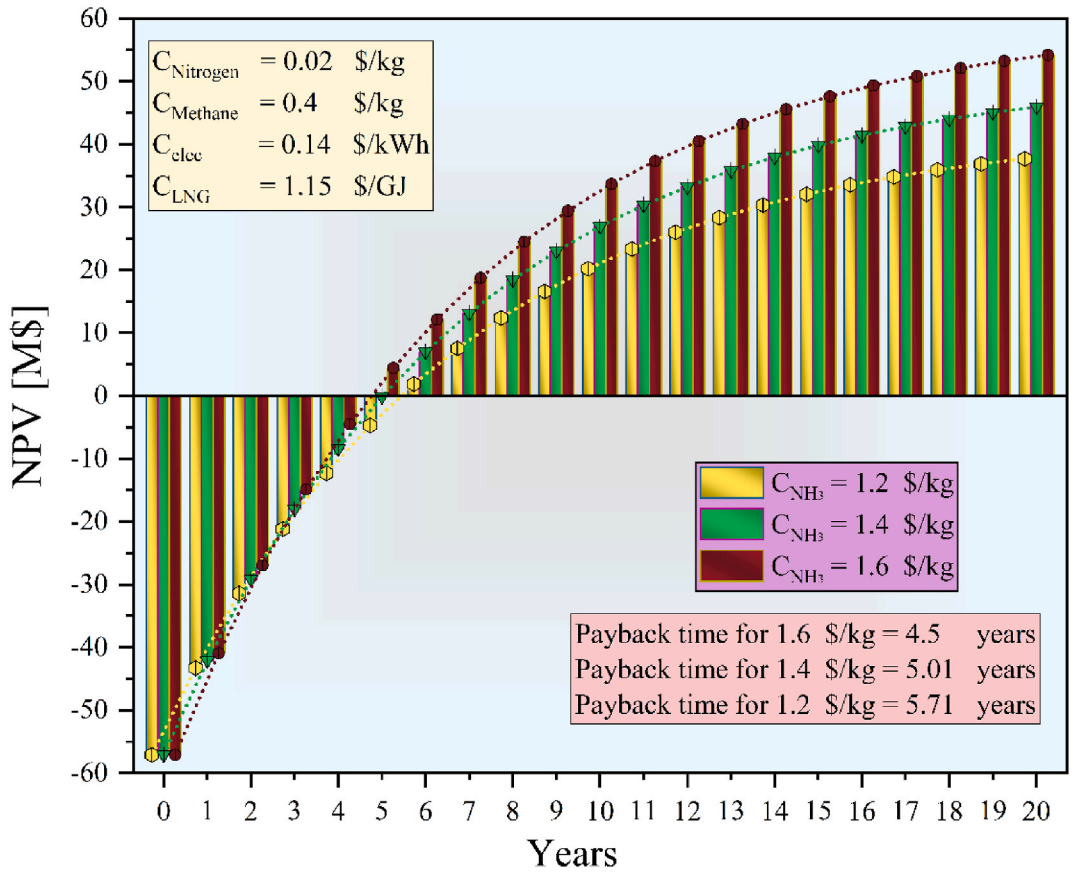

Fig. 11. The NPV of the integrated system evaluated over a 20-year project lifetime for different selling prices of Ammonia.

1.6 $/kg reaches approximately 55 M$, compared to about 50 M$ for 1.2 $/kg. This highlights ammonia's dominant contribution to the project's profitability, emphasizing how sensitive the system's financial viability is to the ammonia market price.

The second NPV analysis that is shown in Fig. 12, examines the impact of varying methane's selling price ($C_{methane}$) at 0.2, 0.4, and 0.6 $/kg, while keeping the prices of other products fixed at 0.02 $/kg for nitrogen, 1.2 $/kg for ammonia, 0.14 $/kWh for electricity, and 1.15

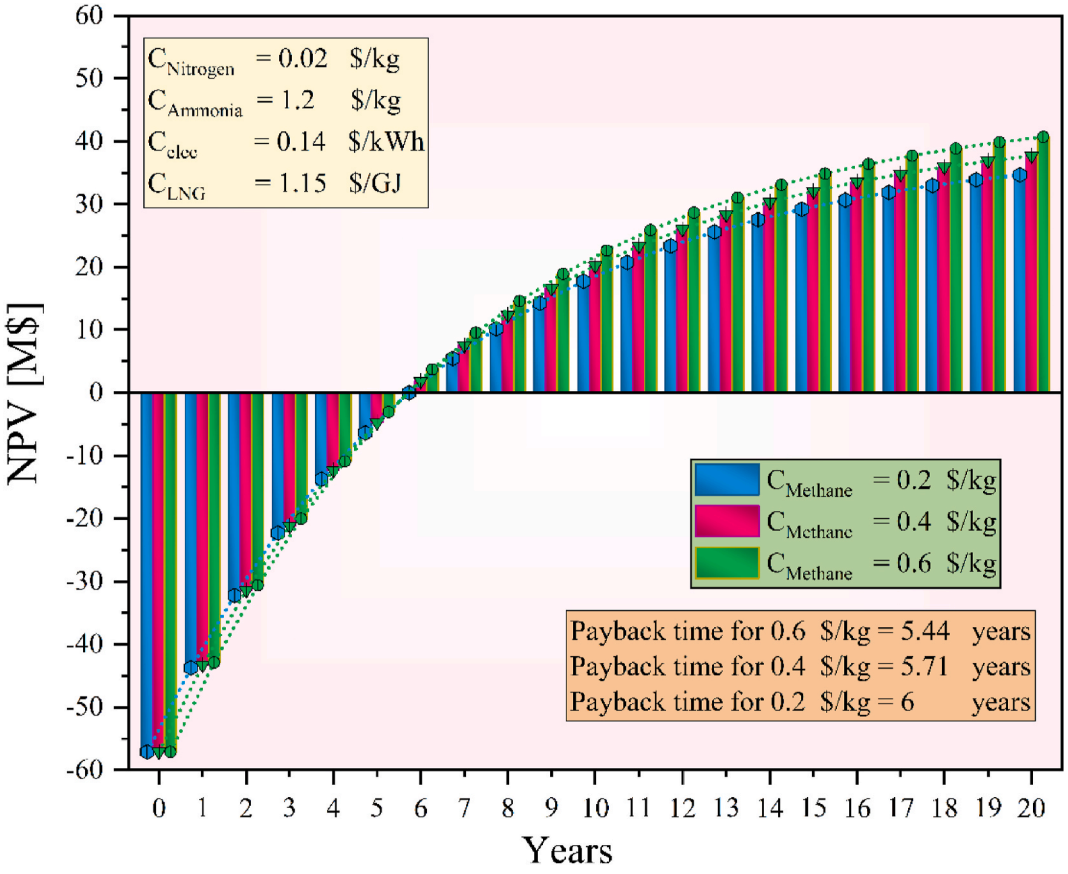

Fig. 12. The NPV of the integrated system evaluated over a 20-year project lifetime for different selling prices of Methane.

$/GJ for LNG. Similar to the first plot, the NPV increases steadily from an initial negative value of around −58 M$ as product sales generate income. The economic effect of methane price variation is evident but less pronounced than ammonia in the first plot. The payback periods for methane prices of 0.6, 0.4, and 0.2 $/kg are 5.44, 5.71, and 6.0 years, respectively. The NPV after 20 years rises from around 50 M$ at 0.2 $/kg to roughly 53 M$ at 0.6 $/kg. Although methane pricing affects profitability and payback time, the variation in final NPV is narrower compared to that caused by ammonia price changes. This confirms that while methane sales enhance the system's revenue stream, ammonia remains the primary driver of financial returns in this configuration.

5.4. Optimization results

In this section, a comprehensive multi-objective optimization analysis is conducted to evaluate the thermoeconomic and environmental performance of the proposed system under various operational scenarios. Three optimization scenarios are formulated to assess the trade-offs between key performance parameters, including Methane and Ammonia production rates, total product cost, exergetic efficiency, and the environmental index. Each scenario focuses on a different set of optimization objectives to capture a broad perspective of system performance.

The first scenario shows optimization results based on environmental index in kg/kWh, exergy efficiency in %, and total product cost in $/kWh. The scattered points map the system's operational behavior under different trade-off conditions between environmental impact, thermodynamic performance, and economic viability. The optimum point identified here features an environmental index of 0.068 kg/kWh, an exergy efficiency of 39.42 %, and a total product cost of 0.107 $/kWh. The graph highlights how configurations with lower environmental impact generally correspond to slightly lower efficiencies and moderate product costs, while the optimal point provides a well-rounded performance across all three dimensions.

The second graph represents the optimization scenario outcomes in terms of methane production rate in kg/s, environmental index in kg/kWh, and total product cost in $/kWh. The distribution of candidate solutions shows the system's performance envelope as methane production increases, typically leading to higher environmental index values and production costs. The optimum solution located via TOPSIS marks a methane production rate of 0.16 kg/s, an environmental index of 0.0702 kg/kWh, and a total product cost of 0.0976 $/kWh. This graph demonstrates that a higher methane output can still be achieved while maintaining relatively low economic and environmental burdens at this optimal configuration.

The third scenario illustrates the optimization results in a three-dimensional plot with total product cost in $/kWh, exergy efficiency in %, and ammonia production rate in kg/s. The scattered data points represent the range of system designs evaluated during optimization, reflecting the trade-offs between economic, energetic, and production performance. The optimum solution, marked on the plot, achieves a total product cost of 0.108 $/kWh, an exergy efficiency of 39.45 %, and an ammonia production rate of 0.488 kg/s. The graph shows that higher ammonia yields can increase product costs and potentially lower efficiency, while the selected optimal point offers a balanced compromise between these criteria.

All three scenarios are represented in a group in Fig. 13(a–c).

A scatter distribution plot is a graphical representation that displays the distribution of solutions or population members in a multi-objective optimization process, showing how decision variables are spread within

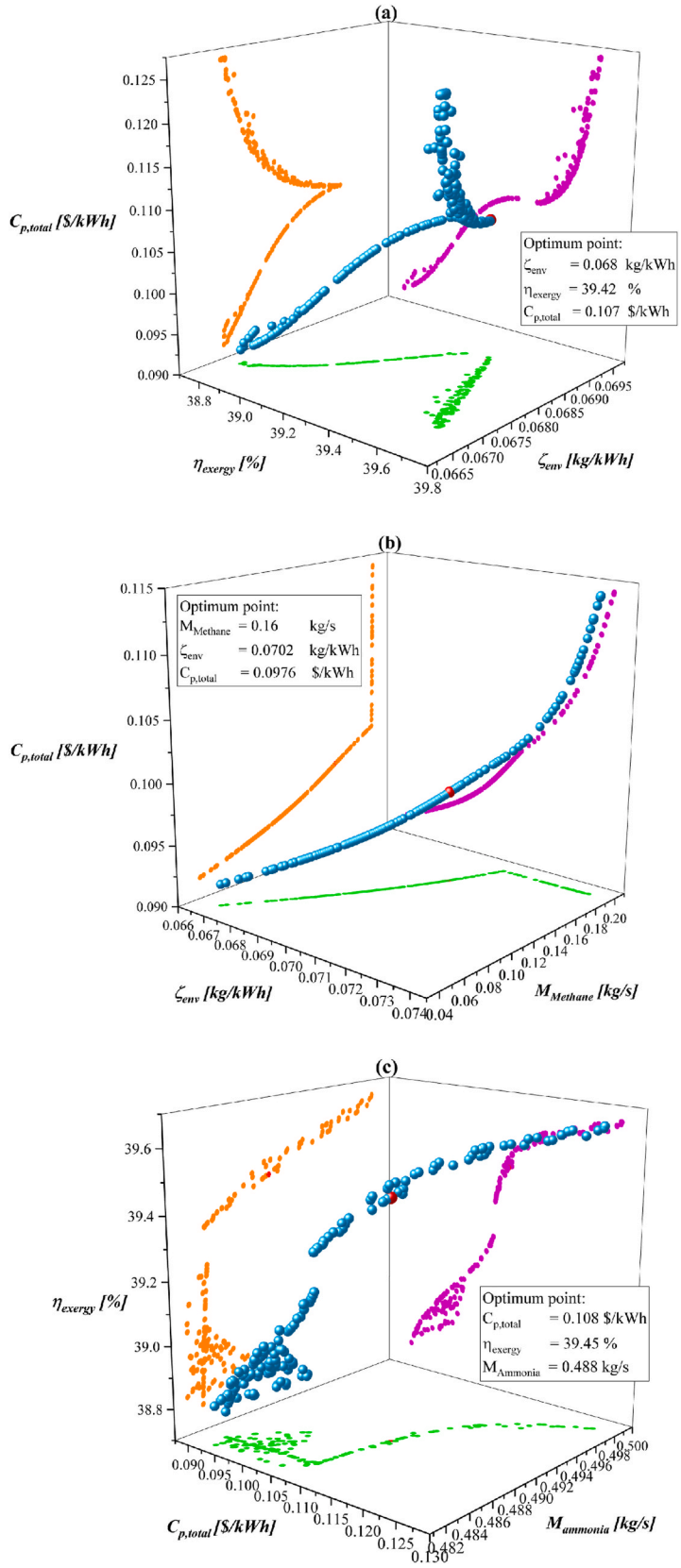

Fig. 13. (a–c). Three optimization scenarios of the integrated cycle based on input data.

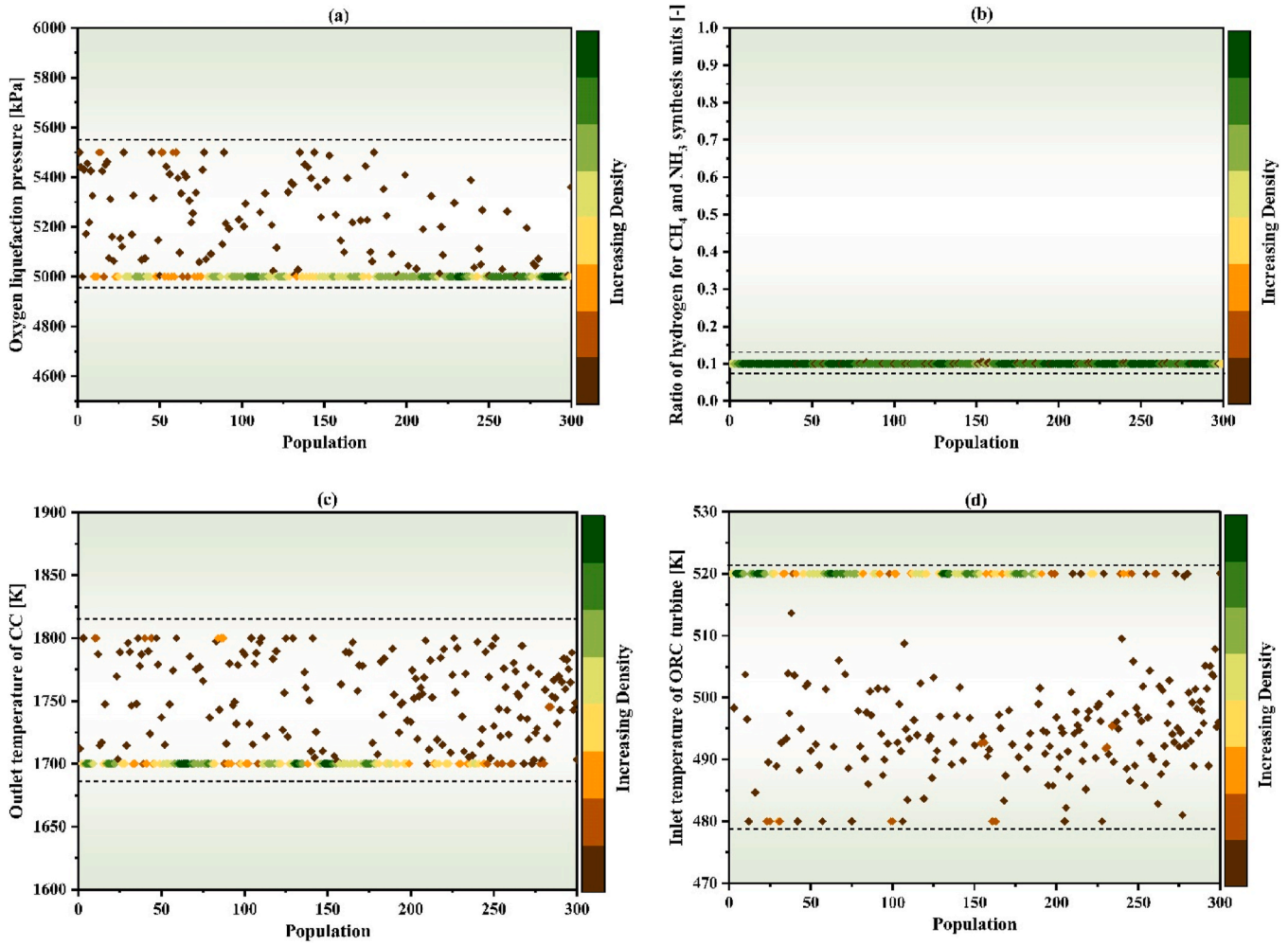

Fig. 14. (a–d). The population distributions for Scenario 1.

the feasible search space. Each point in the plot corresponds to a candidate solution, allowing the identification of regions where optimal solutions are concentrated. Such plots are particularly useful in metaheuristic-based optimization, as they provide insight into convergence behavior, parameter clustering, and trade-offs among decision variables.

For the present study, scatter distribution plots are used to visualize the optimum decision variables for each optimization scenario. The variables considered include: oxygen liquefaction pressure ($P_{liq,O2}$), inlet temperature of the ORC turbine ($T_{ORC,\ turbine}$), hydrogen allocation ratio between methanation and ammonia synthesis units (ratio), and outlet temperature of the combustion chamber (T_{CC}).

Fig. 14(a–d) illustrate the population distributions for Scenario 1, which focuses on maximizing power output and exergetic efficiency while minimizing product cost. In this case, $P_{liq,O2}$ values are strongly clustered around 5000 kPa, the hydrogen ratio stabilizes at 0.1, T_{CC} converges to 1700 K, and $T_{ORC,\ turbine}$ remains at 520 K.

Fig. 15(a–d) present the scatter distributions for Scenario 2, which targets reducing environmental impact while increasing methane production and lowering the unit cost of the product. Here, $P_{liq,O2}$ clusters around 5500 kPa, the hydrogen ratio exhibits flexibility between 0.1 and 0.9, T_{CC} converges to 1700 K, and $T_{ORC,\ turbine}$ is maintained at 520 K.

Fig. 16(a–d) show the population plots for Scenario 3, which aims to maximize exergy efficiency while boosting ammonia production and reducing the unit product cost. In this scenario, $P_{liq,O2}$ values fall within the range of 5000–5500 kPa, the hydrogen ratio is fixed at 0.1, T_{CC} is held at 1700 K, and $T_{ORC,\ turbine}$ remains at 520 K.

5.5. *Comparative performance of the base and optimized scenarios (sensitivity analysis)*

Table 12 reports the decision variables based on parameter sensitivity at the identified optima, key thermodynamic and economic indicators, and the environmental index for the base case and three optimized scenarios. In the base case, the overall exergy efficiency is 38.45 %, obtained from a total fuel-exergy input of 37,635 kW (biomass: 31,523 kW; LNG: 6,112 kW) and useful exergy outputs of 14,473 kW (electricity: 3,804 kW; ammonia: 5,614 kW; methane: 5,055 kW). The levelized unit cost of products is 36.27 $/GJ (≈0.1306 $/kWh), and the (no-capture) emission index is 0.0692 kg/kWh. The base-case production rates are 0.2769 kg/s (NH_3) and 0.101 kg/s (CH_4). The corresponding base-case decision variables are $P_{liq,O2} = 5000$ kPa, $T_{ORC,\ turb} = 500$ K, $T_{CC} = 1800$ K, and hydrogen split ratio = 0.5.

Across the optimized scenarios, exergy efficiency increases to 39.4 %. The total product cost declines from 0.1306 $/kWh (base) to 0.107–0.0976 $/kWh (optimized). The environmental index decreases from 0.0692 kg/kWh to 0.068 kg/kWh, while targeted productivity improvements are achieved: methane rises from 0.101 to 0.160 kg/s,

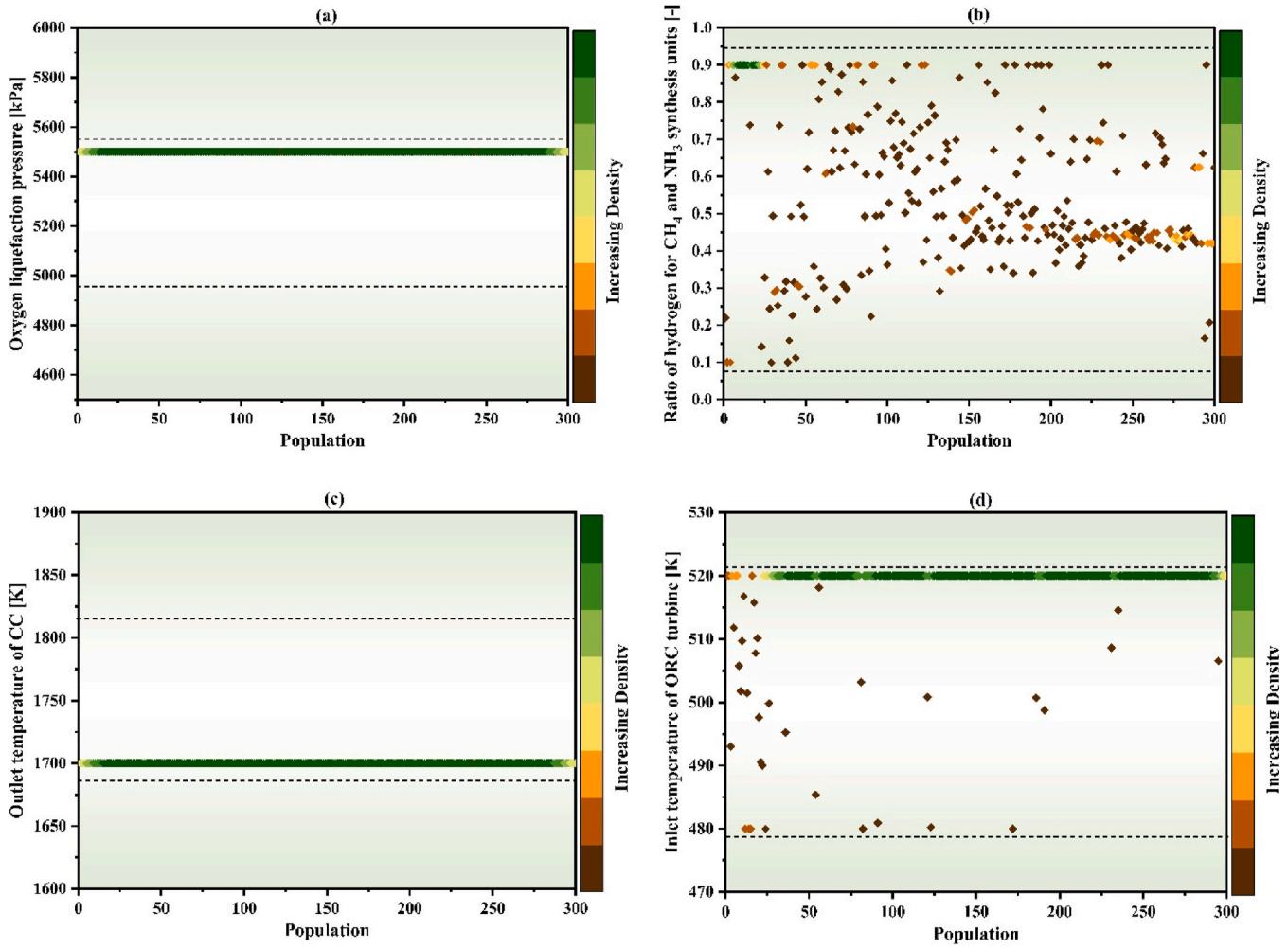

Fig. 15. (a–d). The population distributions for Scenario 2.

and ammonia rises from 0.2769 to 0.488 kg/s.

6. Conclusion

In this study, a comprehensive multi-generation power and fuel production cycle was developed and analyzed, integrating biogas-based oxy-fuel combustion, staged gas turbines, a VCl thermochemical hydrogen production cycle, organic Rankine cycles, cryogenic air separation via LNG cold energy, methanation, and ammonia synthesis units. The system employed three combustion chambers operating in an oxy-fuel configuration with controlled partial combustion and water injection to manage flame temperatures. The oxygen was provided via cryogenic separation, while the exhaust gases, free of nitrogen, facilitated efficient CO_2 and water separation downstream. Hydrogen produced from the thermochemical cycle was directed to methanation, reacting with the captured CO_2, and to an ammonia synthesis unit using separated nitrogen. Additionally, radiative heat losses from the combustion chambers were harnessed via TPV units, enhancing overall system energy recovery. A parametric analysis was performed to investigate the influence of key decision variables on the system's thermodynamic, economic, and environmental performance.

- Increasing the combustion outlet temperature enhances system efficiency and fuel production rates, while offering environmental benefits, albeit with a trade-off of increased operational costs at higher temperature levels.
- Increasing the oxygen liquefaction pressure adversely affects the system's exergy efficiency and fuel production rates while increasing both the total product cost and the environmental index.

Following this, a multi-objective optimization was conducted using the Gray Wolf Optimizer (GWO) algorithm to identify the best trade-offs between exergy efficiency, total product cost, environmental index, ammonia production rate, and methane production rate under three different performance scenarios.

- In the first optimization scenario, targeting ammonia production, the optimal exergy efficiency was obtained at 39.45 %, with a total product cost of 0.108 $/kWh, and an ammonia production rate of 0.488 kg/s.
- The second optimization scenario, focusing on environmental performance (minimizing the environmental index, ζ_{env}), resulted in an optimum point with an exergy efficiency of 39.42 %, an environmental index of 0.068 kg/kWh, and a total product cost of 0.107 $/kWh.
- Lastly, the third optimization scenario, prioritizing methane production, achieved a methane production rate of 0.16 kg/s, with an environmental index of 0.0702 kg/kWh and a total product cost of 0.0976 $/kWh.

These optimization results demonstrated the system's flexibility in meeting different operational goals by adjusting key decision variables.

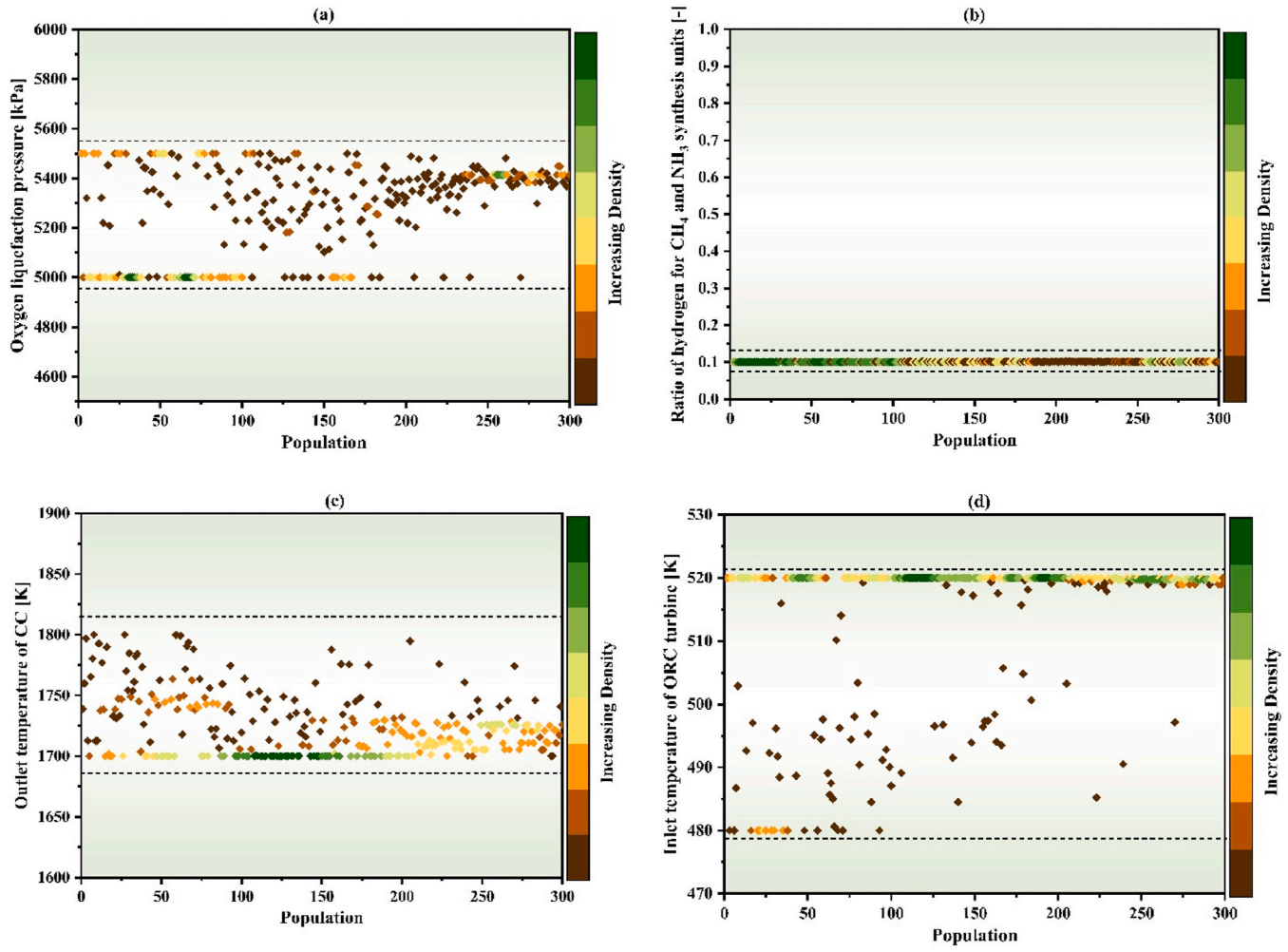

Fig. 16. (a–d). The population distributions for Scenario 3.

Table 12
Comparison of base case and optimized scenarios (decision variables, outputs, cost, and environmental index).

Scenario	$P_{liq,O2}$ [kPa]	T_{CC} [K]	$T_{ORC,\ turb}$ [K]	H_2 ratio [−]	η_{ex} [%]	CH_4 production [kg/s]	NH_3 production [kg/s]	Cost [$/kWh]	Env. index [kg/kWh]
Base case	5000	1800	500	0.5	38.45	0.101	0.2769	0.1306	0.0692
Scenario 1	≈5000	1700	520	0.1	39.42	–	–	0.107	0.068
Scenario 2	≈5500	1700	520	0.1–0.9	–	0.160	–	0.0976	0.0702
Scenario 3	5000–5500	1700	520	0.1	39.45	–	0.488	0.108	–

The study confirmed the technical feasibility and economic competitiveness of this integrated oxy-fuel biogas system while maintaining a low environmental impact, making it a promising approach for clean, multi-product renewable energy systems.

CRediT authorship contribution statement

Shayan Sharafi Laleh: Writing – review & editing, Writing – original draft, Visualization, Validation, Software, Methodology, Formal analysis, Data curation, Conceptualization. **Shayan Rabet:** Software, Methodology, Formal analysis, Data curation. **Haniyeh Sadat Rezaei Mousavi:** Writing – original draft, Validation, Investigation. **Mortaza Yari:** Writing – review & editing, Supervision, Software, Formal analysis. **Saeed Soltani:** Writing – review & editing, Visualization, Supervision. **Ali Saberi Mehr:** Writing – review & editing, Supervision, Resources, Project administration, Investigation, Funding acquisition.

Declaration of competing interest

The authors declare that they have no known competing financial interests or personal relationships that could have appeared to influence the work reported in this paper.

Acknowledgments

This project is supported by a research grant of the University of Tabriz (number 172).

Appendix A. Supplementary data

Supplementary data to this article can be found online at https://doi.org/10.1016/j.energy.2025.138380.

Data availability

Data will be made available on request.

References

[1] Kumar L, Sleiti AK, Hassan I, Rezaei-Gomari S, Azizur Rahman M. Thermo-economic analysis of a novel P2X polygeneration system for hydrogen, ammonia, and methanol production with near-zero emissions. Int J Hydrogen Energy 2025; 150:150201. https://doi.org/10.1016/j.ijhydene.2025.150201.

[2] Yousef MS, Hawwash AA, Santana D. Assessment of a sustainable multigeneration system integrating supercritical CO2 Brayton cycle and LNG regasification: thermodynamic and exergoeconomic evaluation. Case Stud Therm Eng 2024;56: 104205. https://doi.org/10.1016/j.csite.2024.104205.

[3] Tukenmez N, Koc M, Ozturk M. A novel combined biomass and solar energy conversion-based multigeneration system with hydrogen and ammonia generation. Int J Hydrogen Energy 2021;46:16319–43. https://doi.org/10.1016/j.ijhydene.2021.02.215.

[4] Shan S, Zhou Z, Cen K. An innovative integrated system concept between oxy-fuel thermo-photovoltaic device and a Brayton-Rankine combined cycle and its preliminary thermodynamic analysis. Energy Convers Manag 2019;180:1139–52. https://doi.org/10.1016/j.enconman.2018.11.040.

[5] Cao L, Ahmad SF, Rao BN, Ghfar AA, Awan AB, Abou Houran M, et al. Design, multi-aspect investigation and economic advantages of an innovative CCHP system using geothermal energy, CO2 recovery using a cryogenic process, and methanation process with zero CO2 footprint. J Environ Chem Eng 2024;12: 114570. https://doi.org/10.1016/j.jece.2024.114570.

[6] Shan S, Tian J, Chen B, Zhang Y, Zhou Z. Theoretical and technical analysis of the photo-thermal energy cascade conversion for fuel with high-temperature combustion. Energy 2023;263:125990. https://doi.org/10.1016/j.energy.2022.125990.

[7] Eisavi B, Nami H, Ranjbar F, Sharifi A. Economic assessment and optimization of low-carbon biomass-based power, methane, and methanol production. Int J Hydrogen Energy 2024;52:869–88. https://doi.org/10.1016/j.ijhydene.2023.11.025.

[8] Ghiasirad H, Ebrahimian F, Gholizadeh T, Mohammadi A, Mirmasoumi S, Saray RK, et al. LCA and exergy-economic evaluation of a biogas-to-fuels system using CO2 hydrogenation and exhaust gas recycling. Energy Convers Manag X 2025;26:100897. https://doi.org/10.1016/j.ecmx.2025.100897.

[9] Gholizadeh T, Ghiasirad H, Skorek-Osikowska A. Life cycle and techno-economic analyses of biofuels production via anaerobic digestion and amine scrubbing CO2 capture. Energy Convers Manag 2024;321:119066. https://doi.org/10.1016/j.enconman.2024.119066.

[10] Khoshgoftar Manesh MH, Davadgaran S, Mousavi Rabeti SA, Blanco-Marigorta AM. Feasibility study of green ammonia and electricity production via an innovative wind-solar-biomass polygeneration system. Appl Energy 2025;384:125467. https://doi.org/10.1016/j.apenergy.2025.125467.

[11] Pirmohamadi A, Ziapour BM. Investigation of a novel multigeneration system driven by an ammonia-methane Brayton cycle with partial production and utilization of ammonia, methane, and hydrogen: energy and carbon footprint assessments. Heliyon 2024;10:e38769. https://doi.org/10.1016/j.heliyon.2024.e38769.

[12] Chen X, Chen S, Li Q, Yang G, Liu L, Li M, et al. Technical and economic analysis of renewable energy systems with hydrogen-ammonia energy storage: a comparison of different ammonia synthesis methods. J Energy Storage 2025;113:115549. https://doi.org/10.1016/j.est.2025.115549.

[13] Onwuemezie L, Gohari Darabkhani H. Thermophotovoltaics (TPVs), solar and wind assisted hydrogen production and utilisation in iron and steel industry for low carbon productions. J Clean Prod 2024;443:140893. https://doi.org/10.1016/j.jclepro.2024.140893.

[14] Tukenmez N, Yilmaz F, Ozturk M. A thermal performance evaluation of a new integrated gas turbine-based multigeneration plant with hydrogen and ammonia production. Int J Hydrogen Energy 2021;46:29012–26. https://doi.org/10.1016/j.ijhydene.2020.11.054.

[15] Eisavi B, Ranjbar F, Nami H, Chitsaz A. Low-carbon biomass-fueled integrated system for power, methane and methanol production. Energy Convers Manag 2022;253:115163. https://doi.org/10.1016/j.enconman.2021.115163.

[16] Ishaq M, Dincer I. A novel integrated gas-cooled fast nuclear reactor and vanadium chloride thermochemical cycle for sustainable fuel production. J Clean Prod 2024; 468:142853. https://doi.org/10.1016/j.jclepro.2024.142853.

[17] Zhou J, Ashraf Ali M, Hai T, Sharma K, Hama Aziz K, Qasim Ahmed Alyousuf F, et al. Enhanced hydrogen generation in a combined hybrid cycle using aluminum and cooper oxide nanomaterial based on biomass and vanadium chloride cycle: optimization based on deep learning techniques and Environmental appraisal. Int J Hydrogen Energy 2024;52:104–14. https://doi.org/10.1016/j.ijhydene.2022.10.181.

[18] Shan S, Zhou Z, Cen K. An innovative integrated system concept between oxy-fuel thermo-photovoltaic device and a Brayton-Rankine combined cycle and its preliminary thermodynamic analysis. Energy Convers Manag 2019;180:1139–52. https://doi.org/10.1016/j.enconman.2018.11.040.

[19] Safari F, Dincer I. Assessment and multi-objective optimization of a vanadium-chlorine thermochemical cycle integrated with algal biomass gasification for hydrogen and power production. Energy Convers Manag 2022;253:115132. https://doi.org/10.1016/j.enconman.2021.115132.

[20] Cao Y, Zhang N, Zhang X, Bao J, He G. Comprehensive design and 3E analysis of an ORC-based waste heat recovery system with multiple waste heat feeds from ammonia production. Energy Convers Manag 2025;327:119597. https://doi.org/10.1016/j.enconman.2025.119597.

[21] Jalilvand M, Soltani M, Hosseinpour M, Nathwani J, Fitz-Gerald A. Energy and exergy assessment of anaerobic digestion process for ammonia synthesis: toward a sustainable water-energy-food nexus. Biomass Bioenergy 2025;197:107792. https://doi.org/10.1016/j.biombioe.2025.107792.

[22] Müller J, Feldner A, Pröll T, Pfeifer C, Treiber P, Karl J. GreenLNG for Europe – electricity enhanced methanation of biomass. Renew Energy 2025;256:123892. https://doi.org/10.1016/j.renene.2025.123892.

[23] Song Y, Ahmad SF, Abou Houran M, Agrawal MK, Nutakki TUK, Siddiqui MR, et al. Multi-variable study of a novel multigeneration system using biogas separation unit and LNG cold energy utilization, producing electricity, cooling, heat, fresh water, liquid CO2, biomethane, and methanol. Process Saf Environ Prot 2023;180: 616–38. https://doi.org/10.1016/j.psep.2023.10.023.

[24] Shan S, Huang H, Chen B, Wu H, Zhou Z. Performance analysis of biomass driven thermophotovoltaic system from energy and exergy perspectives. Therm Sci Eng Prog 2022;33:101351. https://doi.org/10.1016/j.tsep.2022.101351.

[25] Liang P, Guo Y, Chauhdary ST, Agrawal MK, Ahmad SF, Bani Ahmad AYA, et al. Sustainable development and multi-aspect analysis of a novel polygeneration system using biogas upgrading and LNG regasification processes, producing power, heating, fresh water and liquid CO2. Process Saf Environ Prot 2024;183:417–36. https://doi.org/10.1016/j.psep.2024.01.003.

[26] Xu C, Liu Y, Zhang Q, Xin T, Zhao R, Wang M, et al. Thermodynamic analysis of a novel biomass polygeneration system for ammonia synthesis and power generation using Allam power cycle, vol. 247; 2021.

[27] Fakhari I, Behzadi A, Gholamian E, Ahmadi P, Arabkoohsar A. Design and tri-objective optimization of a hybrid efficient energy system for tri-generation, based on PEM fuel cell and MED using syngas as a fuel. J Clean Prod 2021;290. https://doi.org/10.1016/j.jclepro.2020.125205.

[28] Balta MT, Dincer I, Hepbasli A. Comparative assessment of various chlorine family thermochemical cycles for hydrogen production. Int J Hydrogen Energy 2016;41: 7802–13. https://doi.org/10.1016/j.ijhydene.2015.12.222.

[29] Zhang L, Sobhani B. Comprehensive economic analysis and multi-objective optimization of an integrated power and freshwater generation cycle based on flash-binary geothermal and gas turbine cycles. J Clean Prod 2022;364. https://doi.org/10.1016/j.jclepro.2022.132644.

[30] Dou Z, Zou Y, Mohebbi A. Design and multi-aspect analysis of a geothermal and biomass dual-source power , cooling , heating , and hybrid freshwater production system. Energy 2024;293:130532. https://doi.org/10.1016/j.energy.2024.130532.

[31] Gao Z, Miao J, Zhao J, Mesri M. Comprehensive economic analysis and multi-objective optimization of an integrated gasification power generation cycle. Process Saf Environ Prot 2021;155:61–79. https://doi.org/10.1016/j.psep.2021.09.007.

[32] Meng F, Wang E, Zhang B, Zhang F, Zhao C. Thermo-economic analysis of transcritical CO2 power cycle and comparison with Kalina cycle and ORC for a low-temperature heat source. Energy Convers Manag 2019;195:1295–308. https://doi.org/10.1016/j.enconman.2019.05.091.

[33] Shan S, Zhou Z, Wang Z, Cen K. New oxy-fuel cascade thermo-photovoltaic energy conversion system: effect of cascade design and oxygen ratio. Energy Convers Manag 2019;196:1208–21. https://doi.org/10.1016/j.enconman.2019.06.080.

[34] Magnino A, Marocco P, Santarelli M, Gandiglio M. Economic viability and CO 2 emissions of hydrogen production for ammonia synthesis : a comparative analysis across Europe. Adv Appl Energy 2025;17:100204. https://doi.org/10.1016/j.adapen.2024.100204.

[35] Bailera M, Lisbona P, Romeo LM. Avoidance of partial load operation at coal-fired power plants by storing nuclear power through power to gas. Int J Hydrogen Energy 2019;44:26063–75. https://doi.org/10.1016/j.ijhydene.2019.08.033.

[36] Liu Y, Han J, You H. Exergoeconomic analysis and multi-objective optimization of a CCHP system based on LNG cold energy utilization and flue gas waste heat recovery with CO2 capture. Energy 2020;190. https://doi.org/10.1016/j.energy.2019.116201.

[37] Ghasemzadeh N, Javaherian A, Yari M, Nami H. Energy Conversion and Management : X Thermodynamics modelling and optimisation of a biogas fueled decentralised poly-generation system using machine learning techniques. Energy Convers Manag X 2023;20:100470. https://doi.org/10.1016/j.ecmx.2023.100470.

[38] Ammonia Selling Price 2025. https://www.spglobal.com/commodity-insights/en/news-research/latest-news/energy-transition/051023-interactive-ammonia-price-chart-natural-gas-feedstock-europe-usgc-black-sea (Last access: 09/09/2025).

[39] Natural Gas Price. 2025. https://www.eia.gov/dnav/ng/ng_pri_sum_a_epg0_pin_dmcf_m.htm (Last access: 09/09/2025).

[40] Cell price of LNG. https://www.reuters.com/business/energy/us-natural-gas-prices-climb-2-record-flows-lng-export-plants-2025-03-03/?utm_source=chatgpt.com; 2025.

[41] Bejan A, Tsatsaronis G, Moran MJ. Thermal design and optimization. John Wiley & Sons; 1995.

[42] Bejan A. Advanced engineering thermodynamics. John Wiley & Sons; 2016.

[43] Zhang L, Sobhani B. Comprehensive economic analysis and multi-objective optimization of an integrated power and freshwater generation cycle based on flash-binary geothermal and gas turbine cycles. J Clean Prod 2022;364:132644. https://doi.org/10.1016/j.jclepro.2022.132644.

[44] Sadiq M, khan MS, Abid M, Alkahtani M, Xiaoming B. Exergo-economic analysis of a solar-driven multigeneration system for power, ammonia production, and cooling. Renew Energy 2025;248. https://doi.org/10.1016/j.renene.2025.123072.

[45] Amendola Steven. Thermochemical hydrogen produced from a vanadium decomposition cycle. US Pat No 8,287,838 B2 Washington, DC US Pat Trademark off 2012;2.
[46] The Exergoecology Portal n.d. http://www.exergoecology.com/excalc.
[47] Ferrari C, Melino F, Bosi M. The critical role of emitter size in thermo-photovoltaic generators. Sol Energy Mater Sol Cells 2013;113:20–5. https://doi.org/10.1016/j.solmat.2013.01.031.
[48] Frontera P, Macario A, Ferraro M, Antonucci P. Supported catalysts for CO2 methanation: a review. Catalysts 2017;7:59.
[49] Wei W, Jinlong G. Methanation of carbon dioxide: an overview. Front Chem Sci Eng 2011;5:2–10.
[50] Rönsch S, Schneider J, Matthischke S, Schlüter M, Götz M, Lefebvre J, et al. Review on methanation–From fundamentals to current projects. Fuel 2016;166:276–96.
[51] Hamrang F, Shokri A, Seyed Mahmoudi SM, Ehghaghi B, Rosen MA. Performance analysis of a new electricity and freshwater production system based on an integrated gasification combined cycle and multi-effect desalination. Sustain Times 2020;12:1–29. https://doi.org/10.3390/su12197996.
[52] Gholamian E, Mehr AS, Yari M, Carton JG. Dynamic simulation and techno-economic assessment of hydrogen utilization in dual fuel (Hydrogen/biogas) micro gas turbine systems for a wastewater treatment plant. Process Saf Environ Prot 2023;169:220–37. https://doi.org/10.1016/j.psep.2022.10.045.
[53] Ayres RU, Ayres LW, Martinas K. Eco-thermo-dynamics: exergy and life cycle analysis and Life Cycle Analysis. INSEAD's Cent Manag Environ Resour 1996:49.
[54] Mirjalili S, Mohammad S, Lewis A. Grey wolf optimizer. Adv Eng Softw 2014;69:46–61. https://doi.org/10.1016/j.advengsoft.2013.12.007.
[55] Mahmoudi SMS, Salehi S, Yari M. Three-objective optimization of a novel triple-effect absorption heat transformer combined with a water desalination system. Energy Convers Manag 2017;138:131–47. https://doi.org/10.1016/j.enconman.2017.01.057.